Spectral element modelling of fault-plane reflections arising from fluid pressure distributions

Matthew Haney,[1,*] Roel Snieder,[1] Jean-Paul Ampuero[2] and Ronny Hofmann[3,†]

[1]*Center for Wave Phenomena, Geophysics Department, Colorado School of Mines, Golden, CO 80401, USA. E-mail: mhaney@usgs.gov*
[2]*Institute of Geophysics, Seismology, and Geodynamics, ETH Honggerberg (HPP), Zurich, CH-8093 Switzerland*
[3]*Center for Rock Abuse, Geophysics Department, Colorado School of Mines, Golden, CO 80401, USA*

SUMMARY
The presence of fault-plane reflections in seismic images, besides indicating the locations of faults, offers a possible source of information on the properties of these poorly understood zones. To better understand the physical mechanism giving rise to fault-plane reflections in compacting sedimentary basins, we numerically model the full elastic wavefield via the spectral element method (SEM) for several different fault models. Using well log data from the South Eugene Island field, offshore Louisiana, we derive empirical relationships between the elastic parameters (e.g. *P*-wave velocity and density) and the effective–stress along both normal compaction and unloading paths. These empirical relationships guide the numerical modelling and allow the investigation of how differences in fluid pressure modify the elastic wavefield. We choose to simulate the elastic wave equation via SEM since irregular model geometries can be accommodated and slip boundary conditions at an interface, such as a fault or fracture, are implemented naturally. The method we employ for including a slip interface retains the desirable qualities of SEM in that it is explicit in time and, therefore, does not require the inversion of a large matrix.

We perform a complete numerical study by forward modelling seismic shot gathers over a faulted earth model using SEM followed by seismic processing of the simulated data. With this procedure, we construct post-stack time-migrated images of the kind that are routinely interpreted in the seismic exploration industry. We dip filter the seismic images to highlight the fault-plane reflections prior to making amplitude maps along the fault plane. With these amplitude maps, we compare the reflectivity from the different fault models to diagnose which physical mechanism contributes most to observed fault reflectivity. To lend physical meaning to the properties of a locally weak fault zone characterized as a slip interface, we propose an equivalent-layer model under the assumption of weak scattering. This allows us to use the empirical relationships between density, velocity and effective stress from the South Eugene Island field to relate a slip interface to an amount of excess pore-pressure in a fault zone.

Key words: fault zones, fluid pressures, spectral element method.

1 INTRODUCTION

Seismic data acquisition and processing have evolved to the point that fault-plane reflections are often imaged under favorable conditions (Liner 1999), such as above salt in the Gulf of Mexico. Reflections originating from fault zones hold important information about fluid movement along faults (Haney *et al.* 2005b) and the capacity of a fault to act as a seal (Haney *et al.* 2004). Faults pose a challenge to seismic interpreters by virtue of their dual function as both hydrocarbon traps and pathways (Hooper 1991) for hydrocarbons to move from deep kitchens into shallower, economically producible reservoirs. Any light that seismic data can shed on this situation would be useful.

To gain a stronger grasp on the factors at play in causing fault-plane reflectivity, we have pursued a complete numerical study of seismic wave interaction with fault models. By complete, we do not simply model the entire measured (elastic) wavefield with high fidelity, but additionally process the data into time-migrated images, which is how many geoscientists in the petroleum industry gain access to and begin examining seismic data. We model the wavefield

GJI Volcanology, geothermics, fluids and rocks

933

with a numerical code based on the spectral element method (SEM) that allows for discontinuous slip to occur at fault planes (Ampuero 2002). Processing of the elastic wavefield output by the SEM code has been accomplished using Seismic Un*x (Stockwell 1997).

Previous studies that examined fault-plane reflectivity have relied on simpler or less advantageous numerical methods for forward modelling the seismic wavefield than SEM. For instance, both Jones & Nur (1984) and Moore *et al.* (1995) employed simple 1-D modelling techniques based on the convolutional model of the seismic trace (Robinson 1984) to interpret fault-plane reflections in seismic data. Townsend *et al.* (1998) performed 2-D finite-difference modelling of the seismic wavefield reflected from layers offset by faulting, but did not study the reflections from the fault plane itself. Zhu & Snieder (2002) adapted a 2-D staggered-grid, velocity–stress finite-difference technique to model reflections from a fault or fracture. Bakulin *et al.* (2004) performed 3-D finite-difference modelling over a horizontal fault zone consisting of a network of inclusions, or fractures. The advantages of SEM over finite-difference techniques has been discussed previously by Komatitsch *et al.* (2002).

We sketch the theory behind SEM and, after discussing the dip-filtering step we employ to highlight the fault-plane reflections in migrated data, we present results for several different fault models. These models represent examples and combinations of three basic types of heterogeneity we expect to exist at faults. These three basic types are as follows.

(i) Juxtaposition (sand/shale or shale/sand) contacts.
(ii) Pressure contrasts (ΔP) across the fault.
(iii) Locally weak fault zones, that is, slip interfaces.

We expect from the outset that these various types of heterogeneity show up differently in dip-filtered seismic images. For instance, since the juxtaposition contacts exist over the length scale of a typical bed thickness and have positive (sand/shale) or negative (shale/sand) reflection coefficients, the smoothing of the dip-filter (Oppenheim & Schafer 1975) should act to suppress this contribution to the dip-filtered fault-plane reflectivity compared to the other two fault models. This is desirable since the juxtaposition contacts do not carry direct information on the sealing or conducting properties of the fault.

The other two types of heterogeneity, pressure contrasts and slip at the fault plane, relate to pore-pressure distributions at the fault and are not attacked by the dip filter in the same way as are the juxtaposition contacts. Although reflections due to ΔP are interpreted in the oil industry more commonly than reflections due to a locally weak fault zone, Worthington & Hudson (2000) have recently explained the apparent attenuation of seismic waves transmitted through a fault in the North Sea by allowing slip planes to exist at the fault. In discussing possible causes of interfacial slip, Nihei *et al.* (1994) stated that in 'oil and gas reservoir environments and in parts of the earth's crust where effective stresses may be low due to the presence of high pore-pressures, the contact between neighbouring lithologies or across fractures may be imperfect.' Given this, we expect that a locally pressurized fault zone can act as a slip interface and give rise to reflected seismic waves. Lending importance to the model of a pressurized fault zone, there have recently been reports of field observations of elevated pore-pressure inside fault zones (Crampin *et al.* 2002; Haney *et al.* 2005b).

In the first section of this paper, we discuss empirical relationships between pore-pressure and three basic rock properties—porosity, density and sonic velocity. The data for this analysis come from wells drilled at the South Eugene Island field, offshore Louisiana. These relationships form the basis for the models used in the subse-

quent SEM simulations. The fact that pore-pressure largely controls rock matrix properties in compacting sedimentary basins allows methods for imaging seismic reflections to indirectly measure spatially varying pore-pressure distributions. The variation of the three rock properties with effective stress reveals a fundamental hysteretic type of behaviour in the sediments. Evidence for both plastic (irreversible) and elastic (reversible) deformation exists in the available well data and pressure tests. These two regimes point to different underlying causes of overpressure (Hart *et al.* 1995). For these dual deformation mechanisms, we construct two empirical relationships between each rock property and pore-pressure—one valid for each regime. Before we discuss these issues, though, we wish to clarify exactly what we mean by the term effective stress in the rest of this paper.

2 VERTICAL EFFECTIVE STRESS

Pore-pressures that exceed the hydrostatic pressure, or overpressures, lead to a lowering of density and seismic velocity and may contribute to the reflectivity of associated with fault zones. Pennebaker (1968) was among the first geoscientists to demonstrate the ability of seismic stacking velocities to detect fluid pressures in the subsurface. Terzaghi (1943), however, had previously discussed the basic principle, that of an effective stress acting on the rock frame. According to Terzaghi's principle, the effective stress determines rock properties (e.g. *P*-wave velocity). In extensional regimes typical of sedimentary basins, it turns out that, to a good approximation, only the vertical effective stress needs to be considered since the sediments compact by uniaxial strain (Engelder 1993). Terzaghi's definition of the vertical effective stress, now known as the differential stress σ_d (Hofmann *et al.* 2005), is the difference between the vertical confining stress, σ_v, and the pore-pressure p:

$$\sigma_d = \sigma_v - p. \tag{1}$$

Eq. (1) states that rocks of similar composition but at different confining stress and pore-pressure have the same velocity so long as the difference between the confining stress and pore-pressure is the same. Hence, high pore-pressure, which lowers effective stress, leads to lower seismic velocities.

Following the work of Terzaghi, rock physicists began to question whether the effective stress governing rock properties is simply the difference between the confining stress and the pore-pressure (Wang 2000; Hofmann *et al.* 2005). Today, the most general effective–stress law is instead

$$\sigma_e = \sigma_v - np, \tag{2}$$

where the parameter n is called the *effective stress coefficient*. Carcione & Tinivella (2001) state that the value of n can differ for each physical quantity (e.g. permeability, compressibility, or shear modulus), and that it depends linearly on the differential stress of eq. (1). Currently, the effective–stress coefficient is a controversial topic and is an active area of research within the rock physics community. For the remainder of this paper, we do not distinguish between differential stress, σ_d and effective stress, σ_e; that is, we take $n = 1$ in eq. (2). This assumption is commonly made in the petroleum exploration industry and is supported in arguments posed recently by Gurevich (2004). The assumption of $n = 1$ is also best suited for high porosity, poorly consolidated rocks, as are found in compacting sedimentary basins.

3 POROSITY VERSUS DEPTH

Compaction acts to reduce the porosity of sediments as they are buried; however, this process can continue only as long as fluids in the diminishing pore space are allowed to be expelled. Such would be the case in normally pressured, hydrostatic sediments in which the fluids are in communication up to the seafloor. Once the movement of the fluids out of the pore space is opposed, as in a compartment sealed-off by low permeability or high capillary-entry-pressure shales or fault gouge, the porosity remains constant with burial depth if the fluid is more or less incompressible. This situation is called *undercompaction* (Huffman 2002). Undercompaction means the sediments are 'frozen' in time and are simply buried in their unchanging earlier compaction state (Bowers 1995). To compound the situation, if fluid from outside the undercompacted sediments is pumped into the pore space, or if hydrocarbons are generated from within the undercompacted sediments, a process called *unloading* occurs (Huffman 2002). Whereas undercompaction can only cease the reduction of porosity (Bowers 1995), unloading can actually reverse the trend and increase porosity. Although unloading can reverse the trend, it cannot reclaim all of the previously lost porosity. This is because the compaction process has a large *irreversible* component. In contrast, unloading and loading of sediments by pumping fluid into and then depressurizing the pore space is a reversible process, insofar as the fluid does not cause hydrofracturing.

We have examined wireline data taken in wells at the South Eugene Island field, offshore Louisiana, for indicators of overpressure, such as constant porosity as a function of depth. Previous work by Hart *et al.* (1995) shows the crossover from hydrostatic to overpressured conditions in porosities derived from sonic velocities. We take a slightly different, perhaps more straightforward, approach based on the density log. The South Eugene Island field is a Plio-Pleistocene minibasin formed by salt withdrawal and has yielded more than 300 million barrels of oil in its lifetime. An illustration of the main subsurface features at South Eugene Island is shown in Fig. 1. The main part of the field is a vertical stack of interbedded sand and shale layers bounded by two large growth faults to the north and south.

Fig. 2 shows porosity derived from density logs within the minibasin taken in the following wells at South Eugene Island: A13, A20ST, A14OH, A15, A23, A6, B10, B1, B2, B7 and B8. Because the geology in the minibasin is essentially horizontally layered, we ignore the fact that some wells may be far away from each other and simply look at the depth variation of their porosity. In all the well logs shown in this paper, we have done some smoothing with depth (over ∼100 m) to remove any short-range lithologic influences (e.g. interbedded sand and shale) on the density and velocity. To obtain the porosity from the density log, we take the solid grains to have a density of 2650 kg m^{-3} and the fluid to have a density of 1000 kg m^{-3}, as in Revil & Cathles (2002). In Fig. 2, there is a clear break from the shallow, decreasing porosity trend at a depth of 1800 m. Based on the work of Stump *et al.* (1998), we assume that this is the onset of overpressures in the sedimentary section, beneath a shale bed located above a layer called the JD-sand. We fit an exponential trend to the porosity values above 1800 m, known as Athy's Law (Athy 1930), to get the normal compaction trend in the hydrostatically pressured sediments

$$\phi^c(z) = 0.47\, e^{-0.00046\, z}, \tag{3}$$

where in this equation, the depth z is in metres. The superscript c in eq. (3) refers to the fact that this functional relationship characterizes normal compaction. In the porosity-versus-depth plot of Fig. 2, this
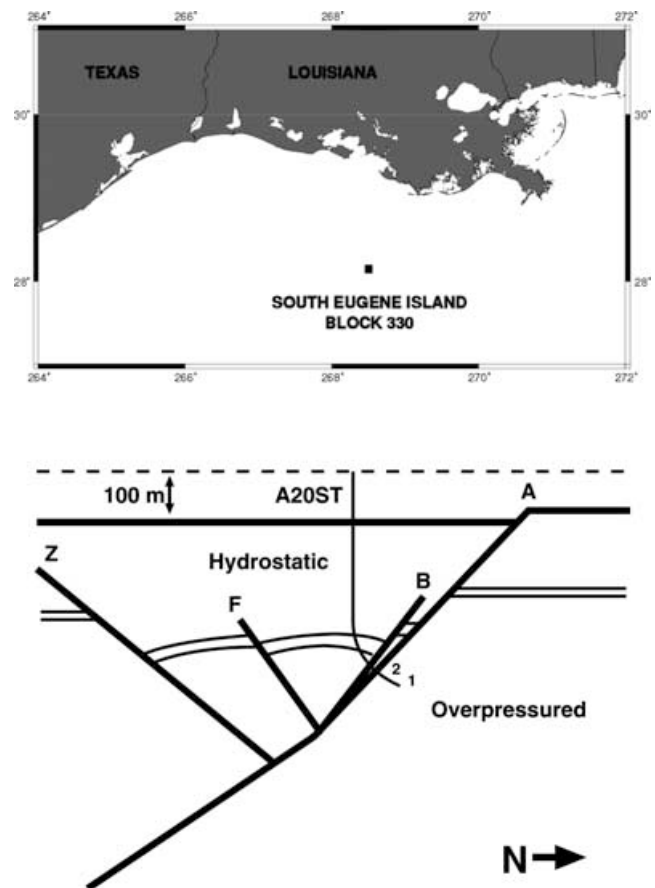

Figure 1. Regional map of the Gulf of Mexico (top) showing the study area, the South Eugene Island field. The four main faults at the field are shown in the qualitative depiction of a typical depth section (bottom) as the A, B, F and Z faults. Throw across the faults is shown by the single layer running from left to right. Most of the wells at South Eugene Island were drilled into the shallow, hydrostatic section within the minibasin, which is bounded by the Z fault to the south and the A- and B-faults to the north. The A20ST well was unusual in that it was continued through the A-fault system and into the deeper, overpressured and upthrown block to the north of the minibasin. There, two pressure measurements (RFTs) were made at the positions shown by 1 and 2 in the depth section.

relationship holds for any movement towards the right on the normal compaction curve and any purely right-going horizontal deviations from the normal compaction curve. For purely right-going horizontal deviations, the depth z used in eq. (3) is equal to the depth at which the horizontal deviation started. The two circles in Fig. 2 represent samples taken in the A20ST well in northern upthrown block (see Fig. 1) and are connected to the normal compaction curve by both horizontal and vertical dashed lines. The vertical dashed lines show the departure of the samples from the normal compaction trend. We return to these in the next section.

The sediments deeper than 1800 m in Fig. 2 maintain a nearly constant porosity of around 0.2 during subsequent burial (a horizontal deviation from the compaction trend). Though the depth of the sediments increases with burial, the effective stress experienced by the sediments does not appear to change and compaction ceases. Hence, the additional weight of the overburden with increasing depth is borne by the fluids trapped in the pore space. As a result, the pore-pressure increases with the vertical gradient of the overburden stress, in order to satisfy Terzaghi's law eq. (1), and is said to have
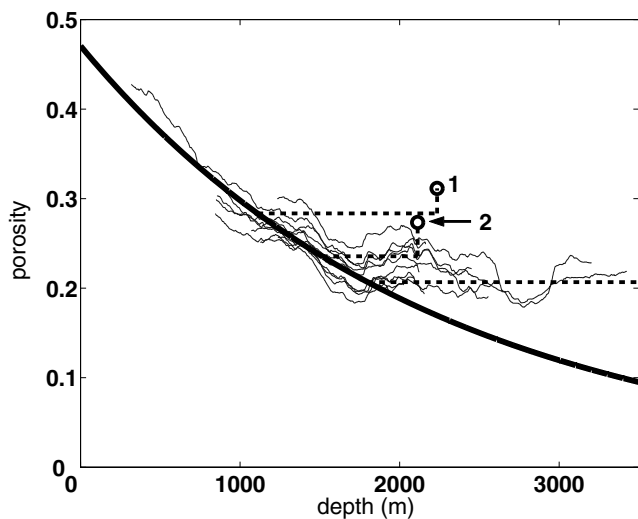
Figure 2. Porosity versus depth at South Eugene Island. The thick, solid line is the best-fitting normal compaction trend using Athy's Law (Athy 1930). The faint solid lines are density-derived porosity values from 11 wells at South Eugene Island. To obtain the porosity, we assume that the solid grains have a density of 2650 kg m^{-3} and the fluid has a density of 1000 kg m^{-3}, as in Revil & Cathles (2002). There is a clear break from the shallow, exponentially decreasing porosity trend at a depth of 1800 m, at which point the porosity remains constant with increasing depth, as shown by the lowest dashed line. The two circles are density-derived porosities from samples in the upthrown block to the north of the minibasin at South Eugene Island (see Fig. 1). The two dashed lines connecting the circles to the main compaction trend are the interpreted porosity histories of the two samples. They show a period of undercompaction, depicted as a horizontal dashed line deviating from the normal compaction trend, followed by an unloading path, shown as a vertical dashed line, due to a late-stage pore-pressure increase.

a *lithostatic gradient*. In doing so, overpressure, or pore-pressure in excess of hydrostatic, is created below 1800 m.

4 DENSITY VERSUS VERTICAL EFFECTIVE STRESS

Since density is a parameter widely used in the field of seismic wave propagation, we study the variability of the bulk density in this section. In contrast to the preceding section, we want to see how density changes with effective stress, not depth. To accomplish this, we take only the measurements that are shallower than 1800 m, where the pore pressure is, by all indications, hydrostatic. Therefore, we know the pore pressure and can calculate the effective stress. In overpressured compartments, since the pore-pressure is unknown, direct measurements by Repeat Formation Tests (RFTs) are necessary to calculate the effective stress.

We rewrite eq. (3) in terms of density and effective stress using the relationships

$$\rho = \rho_s(1 - \phi) + \phi\rho_f, \tag{4}$$

and

$$\sigma_d = \rho_f g z, \tag{5}$$

where ρ is the bulk density and ρ_s and ρ_f are the densities of the solid and fluid components. Note that the relationship for σ_d holds only under hydrostatic conditions. From these relationships and eq. (3), we obtain the normal compaction curve for density

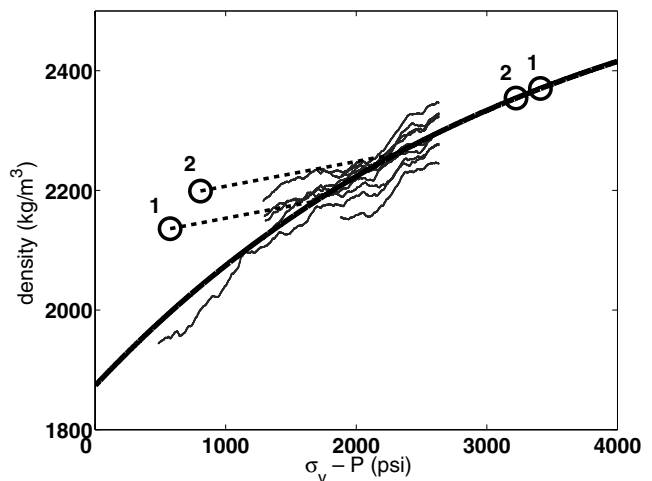$$\rho^c(\sigma_d) = \rho_s - 0.47 (\rho_s - \rho_f) e^{-0.0003\sigma_d}, \tag{6}$$

Figure 3. Density versus effective stress at South Eugene Island. The thick solid line is the same normal compaction trend shown in Fig. 2, except transformed into density and effective stress. The faint solid lines are also the same as in Fig. 2, except that they are now limited to the hydrostatic depths down to 1800 m. The circles represent two pressure measurements, labelled 1 and 2, which were made in the overpressured upthrown block where a density log also existed. For each pressure measurement, we plot the data point twice—one where it should lie on the normal compaction curve were it to have been normally pressured, and the other where it actually does plot because of severe overpressure. Note that sample 1 is from a greater depth than sample 2.

where ρ_s and ρ_f are the densities of the solid and fluid components, taken as 2650 and 1000 kg m^{-3}, respectively, and σ_d is in psi. We plot this normal compaction curve in Fig. 3 together with the density measurements. Also, in Fig. 3, we show as circles two data points obtained from RFT pressure measurements and density log measurements in the overpressured upthrown block. We show the circles in two locations—one on the normal compaction trend where they would plot if the measurements were at hydrostatically pressured locations, and the other where they actually plot because of severe overpressures being present in the upthrown block.

At this point, we don't know exactly how the samples taken in the upthrown block came to be off the normal compaction trend. Using a laboratory measurement of the unloading coefficient by Elliott (1999) on a core sample taken near the locations of samples 1 and 2, the path that these samples took to their present locations can be estimated. Elliott (1999) characterized the effect of unloading, or elastic swelling on the porosity of the core samples to be

$$\phi^u(\sigma_d) = \phi_0 (1 - \beta\sigma_d), \tag{7}$$

where ϕ_0 and β characterize the deviation of the unloading path from the normal compaction trend. Note the superscript u, in contrast to eq. (3), indicating the unloading path instead of the normal compaction trend. Elliott (1999) found that $\phi_0 = 0.37$ and $\beta = 0.98 \times 10^{-8}$ Pa^{-1} for the unloading path. Though these parameters describe the porosity, we use them to find the slope of the unloading path for density using the relationships between porosity and density described earlier. After finding this slope, we can construct the unloading path for the density using eq. (6)

$$\rho^u(\sigma_d) = 0.04 (\sigma_d - \sigma_{max}) + \rho_s$$
$$- 0.47 (\rho_s - \rho_f) e^{-0.0003\sigma_{max}}. \tag{8}$$

This expression contains an extra parameter σ_{max} that refers to the value of the effective stress when the sample began to be unloaded,

or the maximum past effective stress. We do not know $\sigma_{\max}$ for samples 1 and 2, but we do know that $\sigma_{\max}$ must lie on the main compaction trend. Hence, we can construct linear unloading paths for the density, as shown by the dashed lines in Fig. 3. With these unloading paths, we can then find the value for the maximum past effective stress $\sigma_{\max}$. It is worth mentioning that the maximum past effective stress for sample 1 comes out to be $\sim$1500 psi by our approach of using Elliott's experimental results. In an independent measurement, Stump & Flemings (2002) performed uniaxial strain tests on a core sample taken from the same location as sample 1 to find the maximum past effective stress. Stump & Flemings (2002) report a value of 1248 psi for this sample, close to our estimate of $\sim$1500 psi; visually, the discrepancy lies within the error bars of the normal compaction curve's fit to the density log data.

With the estimate of the maximum past effective stress, we can also return to Fig. 2 and find the depth at which samples 1 and 2 left the normal compaction trend, since in the hydrostatic zone the depth is a linearly scaled version of the effective stress. These depths correspond to a slightly lower porosity than that of samples 1 and 2. We interpret this as being the result of a late stage porosity increase and represent it as unloading paths, shown by vertical dashed lines, for samples 1 and 2 in Fig. 2.

5 SONIC VELOCITY VERSUS VERTICAL EFFECTIVE STRESS

For the purposes of modelling faults and to make inferences about the distribution of pore-pressure from seismic interval velocity inversions, accurate pore-pressure-versus-velocity relationships are critical (Dutta 1997). In general, sonic velocity has a normal compaction curve and unloading paths as a function of effective stress that are similar to those we just described for the density well log data. To obtain these relationships for velocity, we proceed as for the density logs: (1) we take 12 shallow wells to make up a data set of sonic velocity versus effective stress; (2) we select the depth range with hydrostatic pressures and plot the sonic velocity versus effective stress; (3) we fit this with a power-law relation for the normal compaction trend and (4) we look at where the two samples from the overpressured upthrown block lie and construct unloading curves using the estimate for the maximum past effective stress we obtained in the previous section. The wells we use for characterizing the sonic velocity come from A20ST, A14OH, A23, A6, B10, B1, B2, B7, B8, A1, B14 and B20.

In Fig. 4, we plot the normal compaction trend for sonic velocity as a thick solid line described by the power-law equation (Bowers 1995)

$$v_p^c(\sigma_d) = 1500 + 2.3\,\sigma_d^{0.77}, \tag{9}$$

where v_p is in m s^{-1} and σ_d is in psi. Note again the superscript c for the normal compaction relation. We also construct the unloading curve for v_p following the relationship first suggested by Bowers (1995)

$$v_p^u(\sigma_d) = 1500 + 2.3\left[\sigma_{\max}\left(\frac{\sigma_d}{\sigma_{\max}}\right)^{1/6.2}\right]^{0.77}, \tag{10}$$

where σ_d and $\sigma_{\max}$ are in psi and v_p is again in m s^{-1}.

To model elastic waves, one other parameter is needed in addition to ρ and v_p; for instance, a seismologist would naturally want the shear velocity. In the absence of information on the shear wave velocity v_s and pressure in the shallow, hydrostatic sediments, we
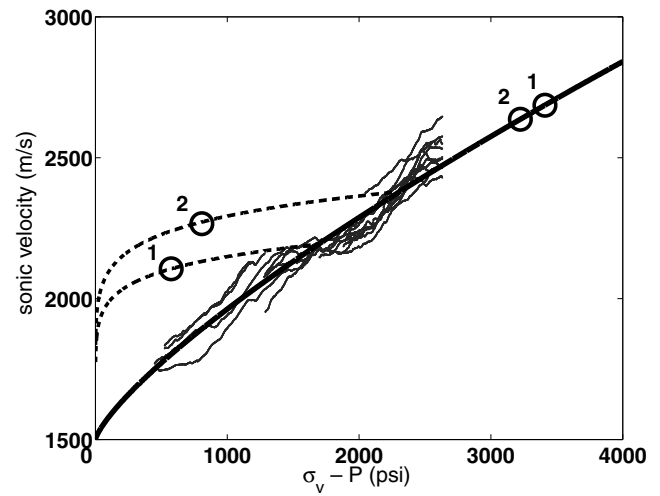

Figure 4. Sonic velocity versus effective stress at South Eugene Island. The thick solid line represents the normal compaction curve fitted to the shallow well data, shown in the faint solid lines. We also plot samples 1 and 2 both where they should fall on the normal compaction trend, were they to be normally pressured, and where they actually plot due to the severe overpressure where they were obtained. Using the estimate for past maximum effective stress from the density plot and the Bowers-type relation (Bowers 1995) shown in eq. (10), we are able to construct the velocity unloading curves, shown as dashed lines.

assume that

$$v_s(\sigma_d) = v_p(\sigma_d) - 1500, \tag{11}$$

where the velocities are in m s^{-1} and the relationship holds on both the normal compaction curve and unloading paths. The data presented by Zimmer *et al.* (2002) for unconsolidated sands supports this assumption, in that the dependence they found for v_s on effective stress is essentially a down-shifted version of the v_p curve. An additional piece of supporting evidence comes from the only v_s data available at South Eugene Island, a shear log from the A20ST well, where samples 1 and 2 were taken (Anderson *et al.* 1994). There, the ratio of v_p/v_s from the sonic and shear logs falls between 3 and 3.5 in the overpressured upthrown block. Inserting the values for v_p at samples 1 and 2 into eq. (11) to get v_s and finding the corresponding ratio of v_p/v_s, we get $v_p/v_s \sim 3.5$ at sample 1 and $v_p/v_s \sim 3.0$ at sample 2, within the range of the ratios observed in the sonic and shear logs.

To summarize, we have established two empirical relationships between each of three basic rock properties and pore-pressure at the South Eugene Island field. Most importantly for subsequent numerical modelling of wave propagation, we have found relationships for the density ρ and the sonic velocity v_p on both the normal compaction and unloading paths. Without shallow information on the shear velocity v_s, we must make the assumption that it is a down-shifted version of the $v_p(\sigma_d)$ relationship. From looking at the density-derived porosity-versus-depth-relationship, we are able to conclude that the deep, overpressured sediments below the JD-sand are predominately overpressured because of undercompaction, since their porosity did not change appreciably with depth. In contrast, both undercompaction and unloading have contributed to the current overpressured state of the sediments on the upthrown side of the minibasin. We assume that the sediments within the minibasin bounding growth fault zones (faults A and B in Fig. 1) are in a similar compaction state as the upthrown block since Losh *et al.* (1999) have stated that these 'fault zones are typically at the

000

same pressure as the upthrown sediments.' Our conclusion that the upthrown sediments have undergone both undercompaction and unloading is in agreement with a previous study by Hart *et al.* (1995) on porosity and pressure at South Eugene Island. We use the above empirical relationships between the elastic parameters and fluid pressure in the following sections to simulate fault-plane reflections from different pressure distributions in the subsurface.

6 THE SPECTRAL ELEMENT METHOD

Numerical modelling of wave propagation in the Earth can be based on the weak (Zienkiewicz & Taylor 2000) or strong forms (Boore 1970) of the elastodynamic equations of motion. By weak and strong, we mean the integrated or differential forms of the equations of motion. SEM is based on the weak form and naturally handles general geometries and exotic boundary conditions. In the finite-difference method (based on the strong form), it is notoriously difficult to implement a linear-slip boundary condition (Coates & Schoenberg 1995) or any general boundary condition for that matter (Boore 1970; Kelly *et al.* 1976). On the other hand, SEM with explicit time-stepping does not require the inversion of a large matrix, a property usually identified with finite-difference methods and lumped-matrix finite-element methods. Formally, this property stems from the diagonality of the mass matrix, a feature that is consistently obtained by design of the SEM through a combination of subintegration and the choice of coincident interpolation and quadrature nodes. Although this design is in contrast to the classical and artificial mass-lumping in FEM, the SEM mass matrix can also be obtained from lumping of the exactly integrated mass matrix (Karniadakis & Sherwin 1999). SEM has the additional property of spectral convergence, meaning that, as the polynomial order of the basis functions is increased, the numerical error goes down exponentially (Karniadakis & Sherwin 1999). The practical implication of spectral convergence is the low number of nodes per wavelength required to reach a given accuracy, as demonstrated by the dispersion analysis of Thompson & Pinksy (1994).

The term 'spectral element' indicates that SEM is a mixture of finite-element and spectral methods (Komatitsch & Vilotte 1998). As a result, there are two parameters relevant to the mesh in SEM: the size of the elements and polynomial degree ($n - 1$, where n is the number of zero crossings of the basis functions used within each element). Komatitsch & Tromp (1999) refer to these parameters when they speak of the global mesh and the local mesh. Concerning the local mesh, there is a known trade-off between accuracy and numerical cost (Seriani & Priolo 1994), which suggests that polynomial

degrees no higher than 10 should be used within the elements. For the numerical examples in this paper, we use a polynomial degree of eight, $n_\ell = 8$.

7 MODELLING FAULTED STRUCTURES

The flexibility provided by SEM makes possible the simulation of seismic data for several fault models. In addition to numerically modelling the full 2-D elastic wavefield, we process the SEM modelled data into its migrated image. Thus, our procedure represents a complete modelling and processing sequence. Fig. 5 depicts the geometry of the basic faulted structure we study. The faulted structure contains several layers and a slip interface confined to the fault plane (see Fig. 5). Different models, discussed shortly, share this same faulted structure but differ in the values of the material properties assigned to the various layers and the slip interface. The faulted structure depicts a normal fault with a vertical throw of 20 m, a value characteristic of a small fault. The normal fault dips at 45°. The faulted structure shown in Fig. 5 is similar to the one previously studied by Townsend *et al.* (1998) to assess changes in seismic attributes caused by faults disrupting the lateral continuity of events. We discuss the material properties used for the different models shortly.

We mesh the interior of the fault structure shown in Fig. 5 using a freely available mesh program developed by INRIA, called EMC2. The program can be downloaded at: http://www-rocq.inria.fr/gamma/cdrom/www/emc2/eng.htm. As discussed in the previous section, SEM has both a local and global mesh. The global mesh is interactively built first using the EMC2 program. Once the global mesh is built, the local mesh is computed automatically within the SEM code. For the examples in this paper, we use a semi-structured global mesh since the faulted structure shown in Fig. 5 is not overly complex. A semi-structured global mesh is desirable, as opposed to an unstructured mesh, since the accuracy of SEM depends on the Jacobian of the transformation between a generally shaped element and a standard rectangular element over which the integration is performed. Although the global mesh we use has structure, it honoors the slanted boundaries of the fault. Note that this would not be possible using a rectilinear 'checkerboard' grid as in finite-difference methods. In that case, the slanted face of the fault would be represented by a 'stair-stepping' pattern. This type of model would give rise to artificial diffractions from the fault plane. After initial construction of the global mesh for SEM, the quadrangle elements comprising the mesh are regularized so that their shapes mimic rectangles as closely as possible. For the faulted
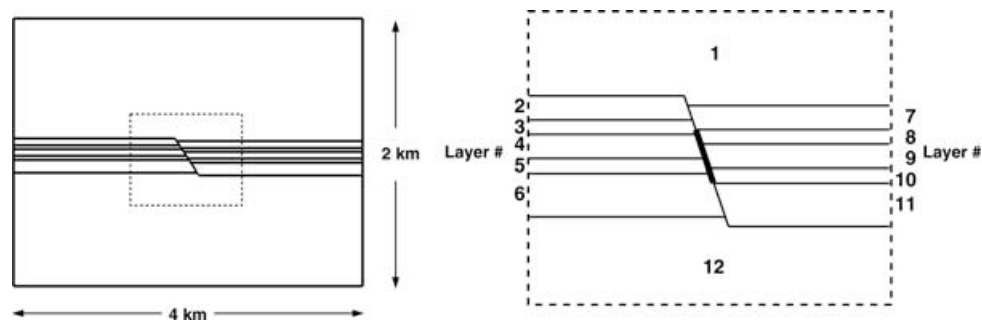

Figure 5. The numerical model (left-hand panel) with a zoom-in of the normal fault (right-hand panel). The zoom area is shown on the numerical model with a dashed rectangle. A seismic survey has been simulated numerically using this model; details of the survey parameters are given in the text. In the zoom, layers are labelled with numbers 1–12 corresponding to the material properties for models listed in subsequent tables. For models with a slip interface at the fault, the portion of the fault plane that slips is shown by a thicker line in the zoom.

structure in Fig. 5, the entire 2 km × 4 km model is made up of 80 × 160 global mesh elements. Thus, the global mesh is made up of quadrangles that are approximately rectangles of dimension 25 m × 25 m. Each global mesh element is further broken down into 64 ($= n_\ell^2$) smaller local elements as defined by the employed polynomial degree ($n_\ell = 8$), as discussed in the previous section.

We simulate a seismic survey over the faulted structure in Fig. 5 using 11 seismic sources. The first source is located 1 km from the leftmost edge of the model and the source array continues for 2 km at a spacing of 200 m (or a 200 m shot interval). In addition to the sources, there are 241 receivers employed in the simulated seismic survey. The first receiver is located 500 m from the leftmost edge of the model and the receiver array continues for 3 km at a spacing of 12.5 m. The receiver array is kept constant when exciting the different sources. We forward model the elastic wavefield by running the SEM code in serial (one compute node for each shot) on a 32-processor pentium IV Xeon (3.0-GHz) cluster. All of the subsequent processing of the modelled wavefield is performed on a workstation using the Seismic Un*x package (Stockwell 1997).

Tables 1 and 2 show the compressional velocity and the density of four models for the faulted structure shown in Fig. 5. These four models represent four different states of overpressure in the foot-wall of the faulted structure. Assuming a hydrostatic pressure of 2800 psi at the depth of the fault, the different overpressure states

Table 1. *P*-wave velocities for models 1–4 used in the SEM simulations. The vertical throw between the upthrown (layers 2–6) and downthrown (layers 7–11) sediments is 20 m. The geometry of the faulted structure is given in Fig. 5. The *S*-wave velocity for each layer is 1500 m s^{-1} less than the *P*-wave velocity, as shown in eq. (11).

Layer	Thickness (m)	v_p (m s^{-1}) Model 1	v_p (m s^{-1}) Model 2	v_p (m s^{-1}) Model 3	v_p (m s^{-1}) Model 4
1	900	2600	2600	2600	2600
2	50	2750	2570	2660	2705
3	30	2600	2380	2490	2545
4	50	2750	2570	2660	2705
5	30	2600	2380	2490	2545
6	90	2750	2570	2660	2705
7	50	2750	2750	2750	2750
8	30	2600	2600	2600	2600
9	50	2750	2750	2750	2750
10	30	2600	2600	2600	2600
11	90	2750	2750	2750	2750
12	850	2600	2600	2600	2600

Table 2. Densities for models 1–4 used in the SEM simulations. The vertical throw between the upthrown (layers 2–6) and downthrown (layers 7–11) sediments is 20 m. The geometry of the faulted structure is given in Fig. 5.

Layer	Thickness (m)	ρ (kg m^{-3}) Model 1	ρ (kg m^{-3}) Model 2	ρ (kg m^{-3}) Model 3	ρ (kg m^{-3}) Model 4
1	900	2240	2240	2240	2240
2	50	2280	2240	2260	2270
3	30	2240	2210	2225	2232
4	50	2280	2240	2260	2270
5	30	2240	2210	2225	2232
6	90	2280	2240	2260	2270
7	50	2280	2280	2280	2280
8	30	2240	2240	2240	2240
9	50	2280	2280	2280	2280
10	30	2240	2240	2240	2240
11	90	2280	2280	2280	2280
12	850	2240	2240	2240	2240

yield pore-pressure contrasts ΔP at the fault of 0 psi (Model 1), 600 psi (Model 2), 300 psi (Model 3) and 150 psi (Model 4). From the model with no pore-pressure contrast (Model 1), it can be seen from Tables 1 and 2 that there are two basic rock types: an acoustically hard shale ($\rho = 2280$ kg m^{-3}, $v_p = 2750$ m s^{-1} and $v_s = 1250$ m s^{-1}) in layers 2, 4, 6, 7, 9 and 11 and an acoustically soft sand ($\rho = 2240$ kg m^{-3}, $v_p = 2600$ m s^{-1} and $v_s = 1100$ m s^{-1}) in layers 3, 5, 8 and 10. The overburden and underburden are given the properties of the sand. The properties of the sand in Model 1 are taken from a well log (in the A20ST well) that intersected a sand layer at the South Eugene Island field known as the JD-sand. The shale values in Model 1 come from the lower bounding shale beneath the JD-sand. The properties of the other three models (2, 3 and 4) are calculated using the pore-pressure relations described earlier for the case of pure undercompaction. Thus, the pore-pressure relations give the numerical modelling a physical basis applicable to the South Eugene Island field. Note that the model with no pore-pressure contrast (Model 1) simply has juxtaposition contrasts across the fault. Thus, by comparing the reflectivity of the four models with different pore-pressure contrasts, we are able to compare reflectivity due to juxtapositions to reflectivity dominated by a strong ΔP at the fault plane. This is relevant to the observed fault-plane reflectivity at South Eugene Island since pressure measurements taken near the large, minibasin-bounding growth fault, known as the A fault, show a 780 psi increase in pore-pressure over 18 m in going from the hydrostatically pressured downthrown sediments to the overpressured upthrown sediments (Losh *et al.* 1999). A fault with such a large and sharp ΔP, compared to the dominant wavelength of seismic waves (~100 m), should reflect the seismic waves due to both the juxtapositions and the ΔP across the fault. By comparing the reflectivity of the four different models, we should be able to estimate how small a pore-pressure contrast can be and still be seismically detectable.

We utilize the advantages of SEM modelling, as described earlier, to accommodate interfacial slip at the fault in addition to the juxtaposition contacts and ΔP across the fault. We chose to implement slip interfaces with a linear slip law: further detail about these slip interfaces is given in Appendix A. In this study, we examine four different values of slip at an interface, as shown in Table 3. The slip interfaces are fully specified in terms of their normal η_N and tangential η_T (or shear) compliances. We adopt a relation between the two compliances given by $2\eta_N = \eta_T$, following Chaisri & Krebes (2000). This relation between the two compliances may also be found in the experimental data of Pyrak-Nolte *et al.* (1990). Specifically, in Table 4 of Pyrak-Nolte *et al.* (1990), the relation $2\eta_N = \eta_T$ is given for sample E30 at a confining stress of 20 MPa and under dry conditions. We refer to the four slip models in order from the most to the least slipping as Slip Model A, B, C and D. Since these slip models only concern the boundary condition at the fault plane, we may insert these different slip models into the pore-pressure models shown in Tables 1 and 2. As an example, we may speak of Slip Model A embedded in Model 1 (the model with no pore-pressure contrast across the fault) and so on. The four models of pore-pressure contrasts (Model 1 through 4) and four models of slip interfaces (Slip Models A–D) thus provide many possible combinations for this SEM modelling study. Note that, for the slip interfaces, the entire fault-plane does not slip—only a portion of it as shown in Fig. 5.

The values for the normal and tangential compliances given in Table 3 are, in general, orders of magnitude larger than those observed in laboratory or field data (Worthington 2006; Worthington & Lubbe 2007). We have selected these values for the compliances so that in our numerical simulations reflections from

Table 3. Four different slip interfaces described in terms of their normal and tangential compliances. These different slip interfaces are used in the SEM modelling.

Slip-Model	Normal compliance, η_N (m Pa^{-1})	Tangential compliance, η_T (m Pa^{-1})
A	5.0×10^{-10}	1.0×10^{-9}
B	3.5×10^{-10}	7.0×10^{-10}
C	2.5×10^{-10}	5.0×10^{-10}
D	1.0×10^{-10}	2.0×10^{-10}

Table 4. Different slip interfaces described in terms of their effective layer parameters assuming a thickness of 10 m and various maximum vertical effective stress, σ_{max}. The estimates are made under the assumption that the fault rock began its unloading path after reaching its maximum vertical effective stress. Relationships between velocity and pore-pressure derived earlier in the paper are used to relate the compliances of the different slip interfaces to vertical effective stress σ_e and pore-pressure p at South Eugene Island. Also the pore-pressure estimate assumes a depth of 1850 m, where the overburden stress is 5500 psi and the hydrostatic pressure is 2800 psi.

Slip-Model	σ_{max}	ρ (kg m^{-3})	v_p (m s^{-1})	σ_e (psi)	p (psi)
A	2800	2200	2020	10	5490
B	2800	2210	2180	90	5410
C	2800	2220	2290	320	5180
D	2800	2270	2470	1660	3850
A	2400	2180	2040	30	5470
B	2400	2190	2190	240	5260
C	2400	2210	2300	780	4730
A	2000	2150	2060	110	5390
B	2000	2170	2200	700	4800
C	2000	2220	2290	1830	3670
A	1600	2120	2080	450	5050

individual slip interfaces are strong enough to show up distinctly. Vlastos *et al.* (2003) adopt a similar approach in their numerical modelling study of fractures. Such large compliances could easily be explained by noting that, for instance, the excess normal compliance is given by the fracture density multiplied by the normal compliance of a single fracture (Worthington & Lubbe 2007). For high fracture densities, as are typically observed at fault zones, the compliances given in Table 3 could, therefore, be realizable since they would represent a high fracture density multiplied by a much smaller (and physically possible) single fracture compliance. As pointed out by Worthington & Hudson (2000) though, such high fracture densities at fault zones are typically complex and are probably not well described by sets of fractures which are aligned and larger than a Fresnel zone. Although the compliances given in Table 3 are unphysically large, as discussed in a following section on the results of our SEM-based numerical simulations, it turns out that we can estimate the responses for smaller values of the compliances since the slip interfaces given in Table 3 are in the weak scattering regime. In the weak scattering regime, the strength of the reflection is, to a high degree of approximation, linearly proportional to the normal and tangential compliances, as described in Appendix A. Thus, in a following section, we linearly extrapolate our numerical results and estimate the minimal values of the compliances that give a notable reflection.

Although the values for the compliances listed in Table 3 are unphysically large, in a later section of this paper we present a weak scattering model to relate the reflections from the slip interfaces to reflections from thin layers. These thin layers represent a simple model of a finite thickness fault zone. Thus, the reflection from a particular slip interface is equivalent to the reflection from a 'family' of thin layers of varying thicknesses and material properties. Given

the properties of these thin layers, we can use the pore-pressure relationships derived earlier to investigate the values of pore-pressure in a finite thickness fault zone which reflects waves equivalently to a slip interface. For now, the values for the compliances listed in Table 3 are simply parameters describing the degree of weldedness between the surfaces on either side of the slip interface.

As with many numerical methods, construction of the global mesh is tied to the material properties (specifically the *P*- and *S*-wave velocities) of the different fault models. For example, it is often quoted that there must be at least 5 gridpoints per minimum desired wavelength for SEM modelling to be accurate and not be corrupted with numerical dispersion (Komatitsch & Tromp 1999). This can be expressed as $\lambda_{min}/(h/n_\ell) \sim 5$. Note that in this criterion the length of the global mesh element h is divided by the polynomial order used for the local mesh n_ℓ. This approximation assumes the local mesh elements are equally spaced within the global mesh element (Komatitsch & Tromp 1999). Since we initiate our simulations with an explosive source whose time function is a Ricker wavelet with a dominant frequency f_0 of 20 Hz, we may take the maximum desired frequency to be 50 Hz, such that $f_{max} = 2.5 f_0$. Since the SEM simulations we perform are elastic, the minimum wavelength λ_{min} is determined by the minimum *S*-wave velocity. The minimum *S*-wave velocity over all of the fault models is, from Table 1, given by 880 m s^{-1} and the minimum wavelength λ_{min} is determined by the minimum *S*-wave velocity divided by the maximum desired frequency. Thus, $\lambda_{min} = 17.6$ m. As stated before, a typical global mesh element has sides of length $h = 25$ m and the polynomial degree employed in the simulations is $n_\ell = 8$. Therefore, at least about 5.6 gridpoints exist per minimum desired wavelength for all of the models.

In addition to the need for 5 gridpoints per minimum desired wavelength, there are also numerical stability considerations. In contrast to numerical dispersion considered above, numerical stability is determined by the *maximum* propagation velocity, which for the elastic SEM code is the maximum *P*-wave velocity of 2750 m s^{-1} (see Table 1). Stability is formally expressed by the CFL-type criterion

$$\frac{v_{max}\Delta t}{h_{min}} \leq 0.5, \tag{12}$$

where Δt is the time step and h_{min} is the minimum length of a local mesh element in the model. Again using the approximation that a global mesh element, with a side of length 25 m broken up into n_ℓ local mesh elements, $h_{min} = 25$ m/8 = 3.125 m for $n_\ell = 8$. Along with the fact that v_{max} is equal to 2750 m s^{-1}, this gives the criteria for a maximum time step to ensure stability as $\Delta t \leq 0.00057$ s. We chose to execute the SEM examples shown in this paper with $\Delta t = 0.0001$ s to ensure stability. We include a safety factor of approximately 5 in our choice of Δt since the value for h_{min} we use is a high estimate: the local mesh elements for SEM are not in fact equally spaced within a global mesh element (Komatitsch & Tromp 1999). This unequal spacing leads h_{min} to be smaller than our earlier estimate. After executing the SEM code with this value

of Δt, we simply down-sample the seismograms by taking every 20th sample to simulate seismic sections with a sampling rate of 2 ms, as is common in the seismic industry.

Since the SEM code is elastic, both primary *PP*-reflections and converted *PS*-reflections show up on the vertical component of the displacement seismograms. We mute the converted waves in order to proceed with conventional *P* wave time-processing. We subtract off the direct waves (*P*, *S* and Rayleigh) by running a homogeneous subsurface simulation with the elastic properties of the overburden (shown as layer 1 in Fig. 5). After this step, we perform a geometrical-spreading correction to compensate for the (approximately) spherical divergence of the wavefront emanating from the source, a normal moveout (NMO) correction to flatten reflections from horizontal layers in a common-midpoint gather (CMP gather), a dip moveout (DMO) correction to flatten reflections from dipping reflectors (e.g. the fault-plane reflection), and finally a summation over different source-receiver offsets for a single CMP (a stack) to simulate zero-offset data (Yilmaz 1987; Black *et al.* 1993). With the simulated zero-offset section, we proceed with a constant-velocity migration using the velocity of the overburden. A source of error in this simulation originates from the slight undermigration of the deepest reflectors and the fault-plane reflection. We chose to migrate with constant velocity since we have interpreted time-migrated seismic sections in the Gulf of Mexico (Haney *et al.* 2004, 2005b) and wanted the modelling and processing sequence to mimic the observed data as closely as possible.

There is one final processing step applied to the migrated data. After producing seismic images, we apply a dip filter in the ω–k domain to highlight the fault-plane reflections relative to the reflections from horizontal layers. We use the following transfer function for the dip filter

$$K(\omega, k) = \frac{1}{2n+1}\left[\frac{2 \sin[(n+1)(\omega p_{st}+k)h/2]}{\sin[(\omega p_{st}+k)h/2]}\right.$$
$$\left.\times \cos[n(\omega p_{st}+k)h/2] - 1\right]. \qquad (13)$$

This is the form of a dip filter that corresponds to stacking $2n+1$ traces centred about an output point along a dip p_{st}. The parameter h is the distance between the traces (assumed constant). An alternative procedure would be a combination of interpolation and slant stacking in the t–x domain; however, the ω–k dip filter is sufficiently accurate for the examples shown here. Fig. 6 depicts the simulated reflection images for the two of the fault models next to their dip-filtered versions which highlight the fault-plane reflection. The dip filter applied to these plots stacks a total of 21 traces and the data and filter have a trace-to-trace spacing of 6.25 m (the midpoint spacing—half of the receiver spacing). This spatial sampling avoids any aliasing problems and attacks all events not having the dip (slope) of the fault-plane reflection. In particular, it attacks the horizontal reflections.

To demonstrate the action of the dip filter, we show both migrated images and their dip-filtered versions in Fig. 6. The panels (a) and (b) of Fig. 6 are for Model 2 and panels (c) and (d) of Fig. 6 are for Slip Model A embedded in Model 1. Panels (a) and (c) of Fig. 6 show the migrated images and panels (b) and (d) show the images in (a) and (c) after dip filtering. Note that the model with a pore-pressure contrast, Model 2, reflects waves much like a traditional seismic interface in that the reflection coefficient is independent of frequency. In contrast, the model with a slip interface, Slip Model A embedded in Model 1, has a reflection coefficient which is approximately the derivative of the incident wave (Chaisri & Krebs 2000). A slice

cut out of the dip-filtered images in the direction perpendicular to the fault-plane (shown as a white arrow in the panels (b) and (d) of Fig. 6) helps in assessing the accuracy of the numerically simulated fault-plane reflections. In Fig. 7, we plot the reflected waveforms together with either the incident wavelet (a 20 Hz Ricker wavelet) in panel (a) or the derivative of the incident wavelet in panel (b), depending on whether the model contains ΔP or interfacial slip at the fault. Note that these plots are in depth—the incident wavelet (or its derivative) has been plotted in depth in Fig. 7 using the local wave speed to make the time-to-depth conversion—and that the amplitudes have been normalized. Thus, the agreement seen between the numerical and predicted waveforms in Figs 7(a) and (b) demonstrates that the SEM modelling, processing and dip-filtering together produce an accurate shape of the reflected waveform from the fault plane. In the next section, we examine reflectivity from the fault plane for combinations of the basic fault models: juxtaposition contacts, pore-pressure contrasts and models with interfacial slip at the fault plane embedded in one of the pore-pressure contrast models. The purpose of this modelling exercise is to study the character of the various types and combinations of reflectivity associated with the fault plane.

8 AMPLITUDES OF WAVES REFLECTED FROM DIFFERENT FAULT MODELS

Although many possible combinations of the different faulted models with ΔP and slip interfaces exist, we chose to highlight two groups of four models in the following which demonstrate the most pertinent information regarding the nature of fault-plane reflections. The first group comprises the four Models (1–4) with different ΔP across the fault and allows the comparison of how different values of ΔP leave their imprint on the fault-plane reflections. The second group comprises the four models with different degrees of interfacial slip at the fault-plane. For this comparison, each of the Slip-Models (A–D) are embedded in a background model given by Model 2 (see Tables 1 and 2). Recall that Model 2 is the model with the maximum amount of ΔP at the fault plane. Thus, embedding the Slip-Models in Model 2 tests to what degree the different slip interfaces show up in the seismic data relative to the maximum amount of ΔP across the fault in the employed models.

In Fig. 8, we plot the maximum reflected amplitude within a small time window (100 ms) of the fault-plane for the four different models of ΔP across the fault: 600 psi (Model 2), 300 psi (Model 3), 150 psi (Model 4) and 0 psi (Model 1—a juxtaposition model). Note that there is not a slip interface at the fault in these examples. All of these amplitude maps are plotted for the cases with (solid line) and without (dashed line) 20 per cent Gaussian additive noise corrupting the migrated images. The plots demonstrate that Gaussian additive noise is efficiently attacked by the dip-filtering step, giving roughly the $1/\sqrt{N}$ attenuation of noise exploited in stacking (Haney *et al.* 2005a). Comparison of the plots shows a roughly linear relation between the reflection amplitudes and the amount of ΔP. As expected, the reflectivity due to the juxtapositions has been dampened by the dip-filtering applied in the direction of the fault-plane. For a pore-pressure contrast as small as 150 psi, it is difficult to tell if a pore-pressure contrast exists at all. Specifically, note the similarity of Figs 8(c) and (d), especially in the degree with which the wobbles due to the juxtapositions contribute to the fault reflectivity. Fig. 9 depicts the zero-offset migrated sections from which these amplitude maps are made. As such, the degree to which the
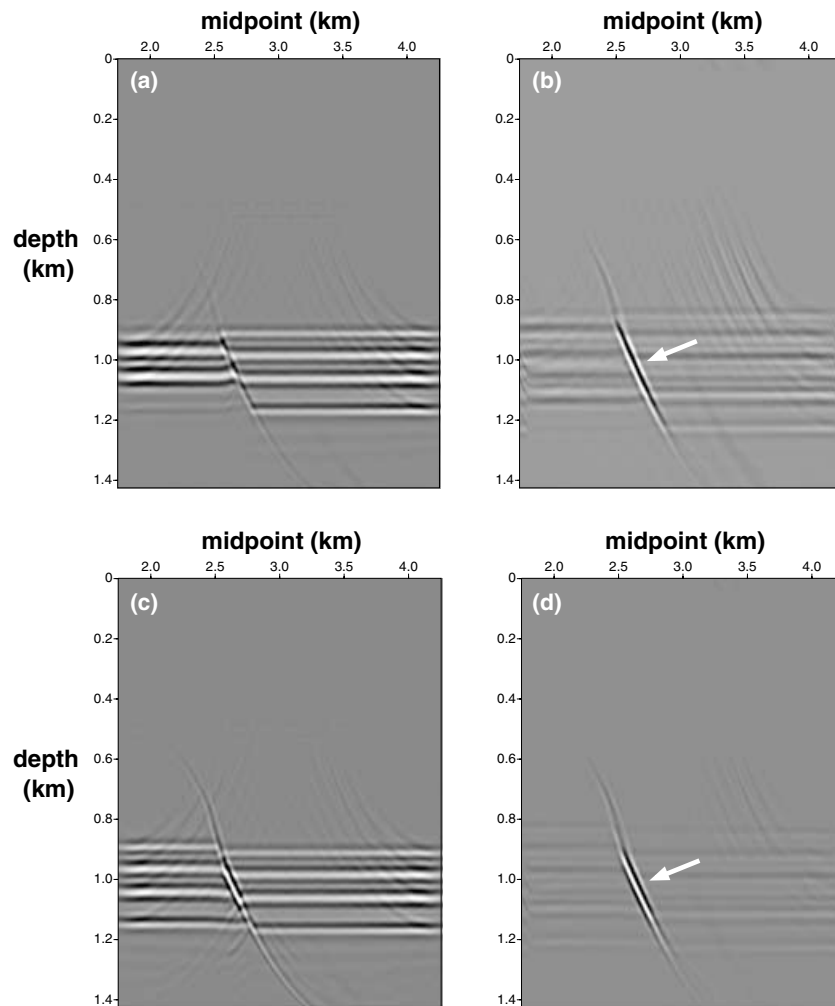
Figure 6. Migrated seismic images are shown in the left-hand panels, (a) and (c) and the same images, after applying dip-filtering to highlight the fault-plane reflections, are shown in the right-hand panels, (b) and (d). Panels (a) and (b) are for Model 2—a pore-pressure contrast across the fault (see Table 1). Panels (c) and (d) are for Model 1—no pore-pressure contrast across the fault (see Table 1). Although there is no pore-pressure contrast in panels (c) and (d), the fault plane is a slip interface. The parameters describing the slip interface are referred to as Slip model A (see Table 3) and, hence, we refer to the model used in panels (c) and (d) as Slip model A embedded in Model 1. The traces in Fig. 7 are sliced from these images in a direction normal to the fault-plane, as shown by an arrow in the dip-filtered images. The horizontal events in the upper panels appear to be not as well suppressed as in the lower panels simply because the fault-plane reflection is stronger in the bottom panel and, as a result, the maximum amplitude of the display is higher.

fault-plane reflections show up in the zero-offset migrated sections prior to dip-filtering in the direction of the fault-plane can be assessed.

In Fig. 10, we again plot the maximum reflected amplitude within a small time window (100 ms) of the fault-plane for Slip-Models A, B, C and D. As discussed before, these Slip-Models are embedded in a background model given by Model 2. From Fig. 10, it is seen that the amplitude of the fault-plane reflection attributable to interfacial slip is reduced as the normal and shear compliances are decreased in going from Slip-Model A to D. The reduction in reflected amplitude is roughly linear in proportion to the reduction of the compliances. This occurs because the reflection coefficient is proportional to the compliance for a relatively weakly slipping interface, as shown in eq. (A6) of Appendix A.

The linearization employed in the derivation of eq. (A6) in Appendix A is valid for the Slip-Models considered here because the *dimensionless* shear and normal compliances of the interfaces are

considerably less than unity. The dimensionless compliance, and not compliance itself, is the measure of how strongly reflecting a slip interface is, since the dimensionless compliance accounts for different frequencies of the incident wave and different local material properties. From Appendix A, we know that the dimensionless normal compliance is $\omega \eta_N \rho \alpha \sec \theta$, where ω is the dominant frequency of the incident wave (20 Hz), η_N is the normal compliance, ρ is the average density across the interface, α is the average *P*-wave velocity across the interface and θ is the incidence angle. For normal incidence ($\theta = 0°$), an average density $\rho = 2260$ kg m^{-3} and an average *P*-wave velocity $v_p = 2700$ m s^{-1}, the dimensionless normal compliance varies between 0.38 and 0.08 for Slip-Models A–D. When this dimensionless number is less than unity, we may expect the strength of the reflections to be linear as a function of the compliance, as observed in Fig. 10 for the Slip-Models. Similarly for tangential case, the dimensionless tangential compliance is $\omega \eta_T \rho \beta \cos \theta$. For normal incidence ($\theta = 0°$), an average
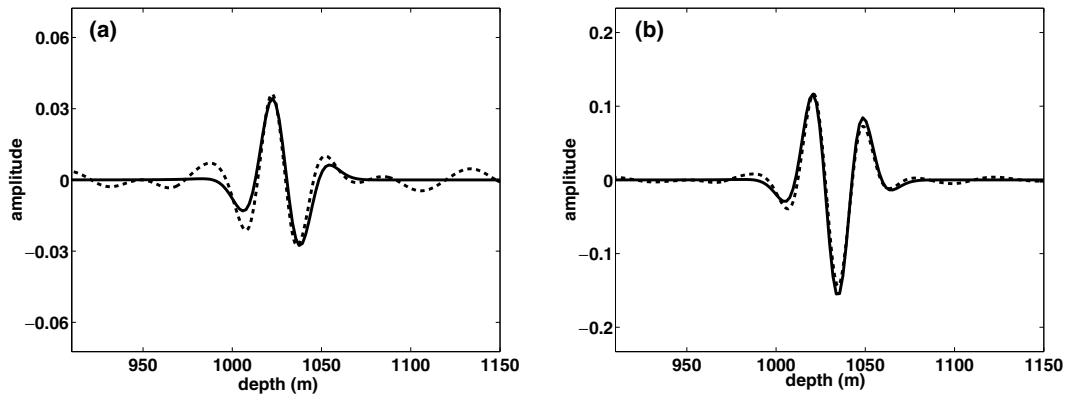
Figure 7. In panel (a), the reflected wave from Model 2, a pore-pressure contrast, is shown as a dashed line. The reflected waveform for Model 2 should be the incident wavelet, which is plotted in panel (a) as a solid line for comparison with the numerical result. In panel (b), the reflected wave from Slip-Model A embedded in Model 1, a fault with a slip interface, is shown as a dashed line. The reflected waveform for Slip-Model A embedded in Model 1 should be the derivative of the incident wavelet, which is plotted in panel (b) as a solid line for comparison with the numerical result. The reflected waveforms for the two models shown in panels (a) and (b) are different in shape since a pore-pressure contrast acts like an all-pass filter in reflection, and a slip interface acts like a high-pass filter.
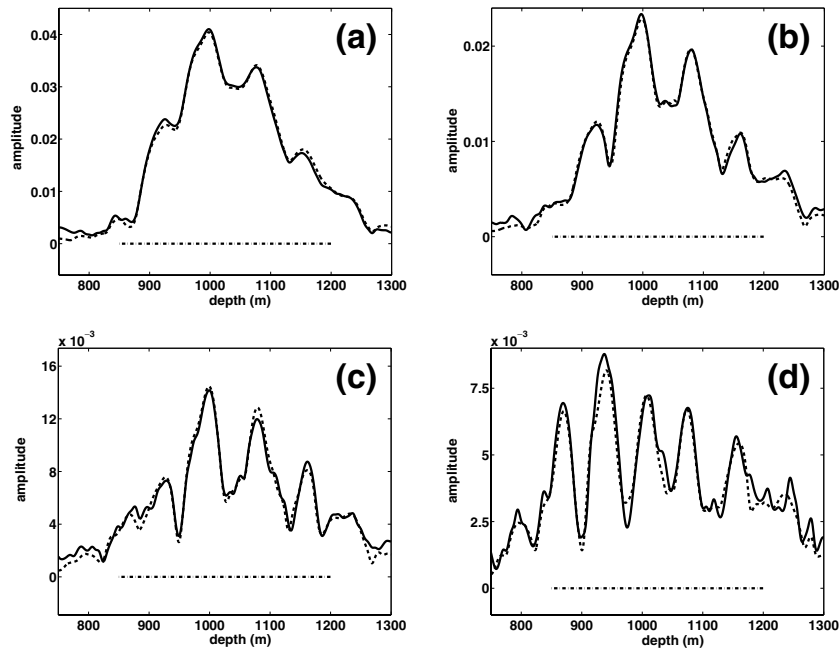
Figure 8. Amplitude along fault-plane for Model 2 in panel (a), Model 3 in panel (b), Model 4 in panel (c) and Model 1 in panel (d). See Tables 1 and 2 for a description of the different Models. These amplitude maps are plotted both with (solid line) and without (dashed line) 20 per cent Gaussian additive noise. The amplitude is plotted as a function of depth on the fault-plane and the extent of the fault-plane is shown with a horizontal line in the bottom portion of each plot. These models represent the situations of: 600 psi pore-pressure difference across the fault (a), 300 psi pore-pressure difference across the fault (b), 150 psi pore-pressure difference across the fault (c) and 0 psi pore-pressure difference across the fault; in other words, the juxtaposition contact model (d). There is not a slip interface at the fault in these examples.

density $\rho = 2260$ kg m^{-3} and an average S-wave velocity $v_p = 1200$ m s^{-1}, the dimensionless tangential compliance varies between 0.34 and 0.07 for Slip-Models A–D. Thus, it is entirely expected that the reflection amplitudes scale linearly with compliances in Fig. 10.

For the smallest compliance, Slip-Model D, the magnitude of the reflection is on the same order as that of the reflection caused by the ΔP present in Model 2 (600 psi). Such a similarity is seen by comparing Figs 8(a) and 10(d). Thus, the degree of slip in Slip-Model D would seem to be a lower limit of compliance for indications of

interfacial slip to appear when $\Delta P = 600$ psi across the fault. Fig. 11 depicts the zero-offset migrated sections from which the amplitude maps in Fig. 10 are made. The reflections due to the interfacial slip at the fault-plane can clearly be made out even without the dip-filtering step.

As demonstrated by Fig. 8, a linear relation may be assumed between the magnitude of the fault-plane reflection due to a ΔP and the value for ΔP itself. This linear behaviour is due to the fact that the values of ΔP considered here do not drastically modify the elastic parameters across the fault. That is, the changes in the elastic
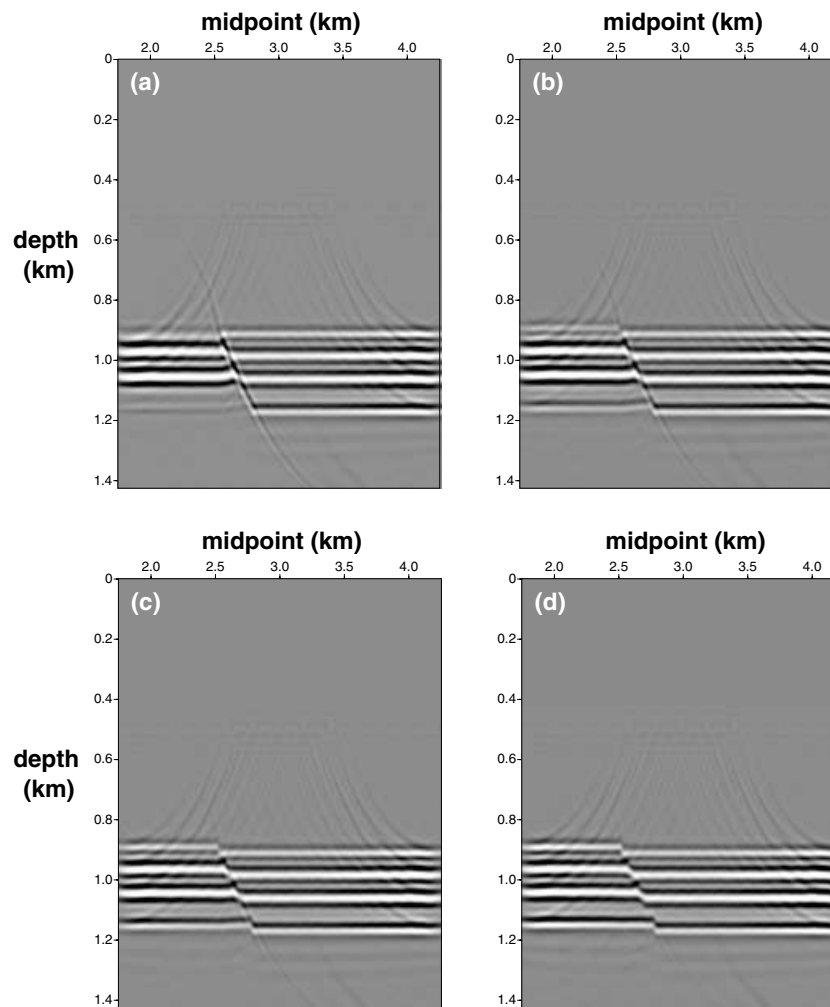
Figure 9. Zero-offset migrated sections for Model 2 in panel (a), Model 3 in panel (b), Model 4 in panel (c) and Model 1 in panel (d). See Tables 1 and 2 for a description of the different Models. The amplitude plots along the fault plane in Fig. 8 are derived from these zero-offset sections after dip-filtering.

parameters across the interfaces divided by their average values across the interface, $\Delta\alpha/\alpha$, $\Delta\beta/\beta$ and $\Delta\rho/\rho$, are less than unity. Since a linear relation also exists between the degree of interfacial slip and the strength of reflection, we can estimate the minimal degree of slip for a reflection from a slip interface to show up in the presence of juxtapositions only (when $\Delta P = 0$ psi). Given that Slip-Model D is the minimal amount of slip for notable reflections in the presence of a $\Delta P = 600$ psi (Model 2), a slip interface with shear and normal compliances reduced by one-fourth of those in Slip-Model 4 would constitute the threshold for indications of interfacial slip to appear in Model 4, when $\Delta P = 150$ psi across the fault. As also demonstrated by Fig. 8, fault reflectivity from pure juxtapositions (Model 1, $\Delta P = 0$ psi) are roughly half as strong as in the case of $\Delta P = 150$ psi. Thus, a slip interface with shear and normal compliances reduced by one-eighth of those in Slip-Model 4 would constitute the threshold for indications of interfacial slip to appear when $\Delta P = 0$ psi across the fault. From Table 3, such a minimally (seismically) visible slip interface would have $\eta_N = 1.25 \times 10^{-11}$ m Pa^{-1} and $\eta_T = 2.5 \times 10^{-11}$ m Pa^{-1}. Reflections from individual slip interfaces with compliances less than these values would be impossible to make out in the presence of the reflectivity due to juxtapositions at the fault-plane, given the typical elastic properties for sands and shales at South Eugene Island field.

9 RELATING SLIP INTERFACES TO A PRESSURIZED FAULT

The slip interfaces used in the numerical modelling and shown in Table 3 do not, up to this point, have any physical meaning in terms of the pore-pressure locally at the fault. In this section, we relate a slip interface to an effective-layer model that demonstrates much of the same wave-scattering behaviour. Thus, a single slip interface can thought to model a 'family' of thin layers with varying elastic properties and thicknesses. With an effective thin layer described in terms of its thickness, density and velocity, the empirical relationships between effective stress and density and effective stress and velocity we derived earlier can lend the slip interfaces physical meaning in terms of pore-pressure. Note that, in what follows, the relationships we derive for compliance of an effective thin layer should not be interpreted physically in terms of an actual fracture. What we are doing here is simply relating a slip interface to a family of thin layers in terms of the similarity of their reflected waveforms.

The derivation presented here is for normally incident *P* waves; we focus on normally incident *P* waves since the seismic imaging discussed in previous sections utilized *PP*-scattered waves at small incidence angles. In fact, for a given spreadlength of a seismic survey, the incidence angles for a fault plane reflection are smaller than
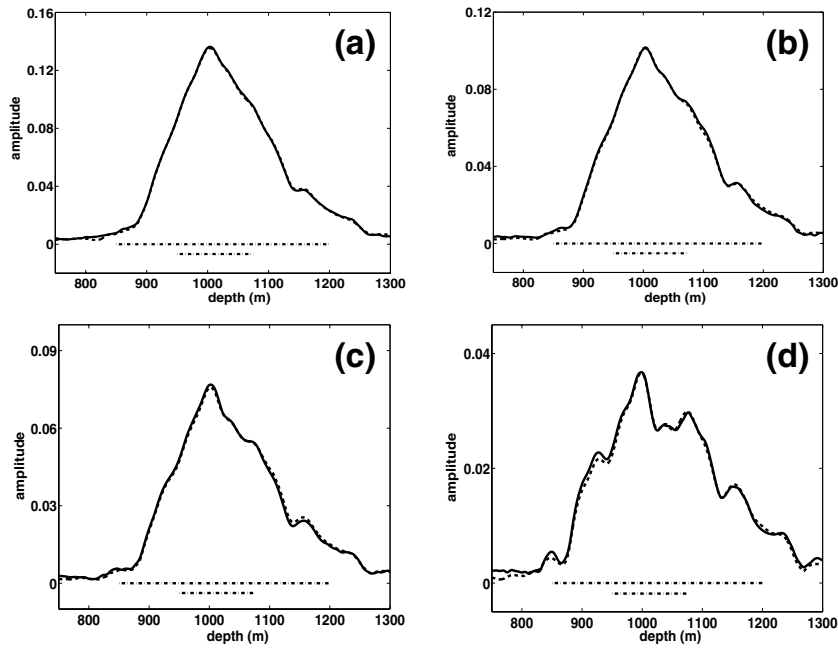
Figure 10. Amplitude along fault-plane for Slip-Model A in panel (a), Slip-Model B in panel (b), Slip-Model C in panel (c) and Slip-Model D in panel (d). See Table 4 for a description of the different Slip-Models. All Slip-Models shown here are for a fault embedded in Model 2 (see Tables 1 and 2) having a pore-pressure contrast of 600 psi across the fault. These amplitude maps are plotted both with (solid line) and without (dashed line) 20 per cent Gaussian additive noise. The amplitude is plotted as a function of depth on the fault-plane and the extent of the fault-plane is shown with a long horizontal line in the bottom portion of each plot. The subportion of the fault where interfacial slip occurs is shown beneath this line with a shorter horizontal line. The maximum amplitude occurs near the centre of the slipping portion of the fault in each slip-model. The amplitude map resembles a triangle since it is, roughly speaking, the convolution of two boxcar functions: the slipping portion of the fault-plane and the dip filter. In moving from Slip-Model A to D, the compliance of the fault slip becomes smaller and, as a result, the reflection magnitude scales in the same proportion, as predicted by eq. (A6) in Appendix A for a weakly slipping interface. The different Slip-Models invoke slip at the fault to represent weakness due to elevated pore-pressure.

those for a horizontal interface at the same depth. Our effective-layer model begins from a weak scattering assumption. For a thin layer, if the interface reflection coefficients at the upper and lower boundary are small, then the entire series of reverberations (Aki & Richards 1980) within the layer can be neglected. The total reflection coefficient from the thin layer can thus be approximated simply as the sum of the reflections off the upper and lower interface. For the case when the thin layer is sandwiched between two identical media,

$$R_{\text{tot}} \approx R_{PP} - R_{PP} \ \exp\left(\frac{2i\omega h}{\alpha_L}\right), \qquad (14)$$

where R_{PP} is the P wave to P wave (PP) reflection coefficient at the upper interface (the reflection at the lower interface is $-R_{PP}$), ω is the frequency, h is the thickness of the thin layer, and α_L is the P-wave velocity in the thin layer. In eq. (14), we have assumed that the impedance difference between the thin layer and the host medium is small enough that the transmission coefficients in moving from the host medium into the thin layer and vice versa are close to 1. This is consistent with the weak-scattering assumption.

The next approximation relies on the layer being sufficiently thin. If, for the argument of the exponential term in eq. (14),

$$\frac{2\omega h}{\alpha_L} \ll 1, \qquad (15)$$

then the exponential can be expanded to first order in a Taylor series

$$\exp\left(\frac{2i\omega h}{\alpha_L}\right) \approx 1 + \frac{2i\omega h}{\alpha_L}. \qquad (16)$$

Note that the condition in eq. (15) states that $1 \gg 4\pi h/\lambda_L$, where λ_L is the wavelength of the wave in the thin layer. Hence, the condition

means that only a fraction of a wavelength fits in the layer. Inserting the Taylor series approximation into eq. (14) gives

$$R_{\text{tot}} \approx -R_{PP} \ \frac{2i\omega h}{\alpha_L}. \qquad (17)$$

This expression shows that the total reflection from a thin weak layer is proportional to the derivative of the incident wave. Widess has discussed this fact in a paper on vertical seismic resolution (Widess 1973).

From eq. (A6) in the Appendix, the normal incidence PP reflection coefficient for a weakly slipping interface between two identical media (the host medium) is

$$R_{PP}^s \approx \frac{i\omega\eta_N\rho\alpha}{2}, \qquad (18)$$

where ω is the frequency, η_N is the normal compliance, ρ is the density of the host medium, α is the P-wave velocity of the host medium, and the superscript s indicates that this is the reflection coefficient for a slipping interface. This equation comes with its own assumption, namely that the dimensionless normal compliance is much smaller than 1, $\omega\eta_N\rho\alpha \ll 1$. Equating this expression to eq. (17) gives

$$\frac{i\omega\eta_N\rho\alpha}{2} = -R_{PP} \ \frac{2i\omega h}{\alpha_L}. \qquad (19)$$

By canceling common factors and solving this for η_N, the normal compliance, we get

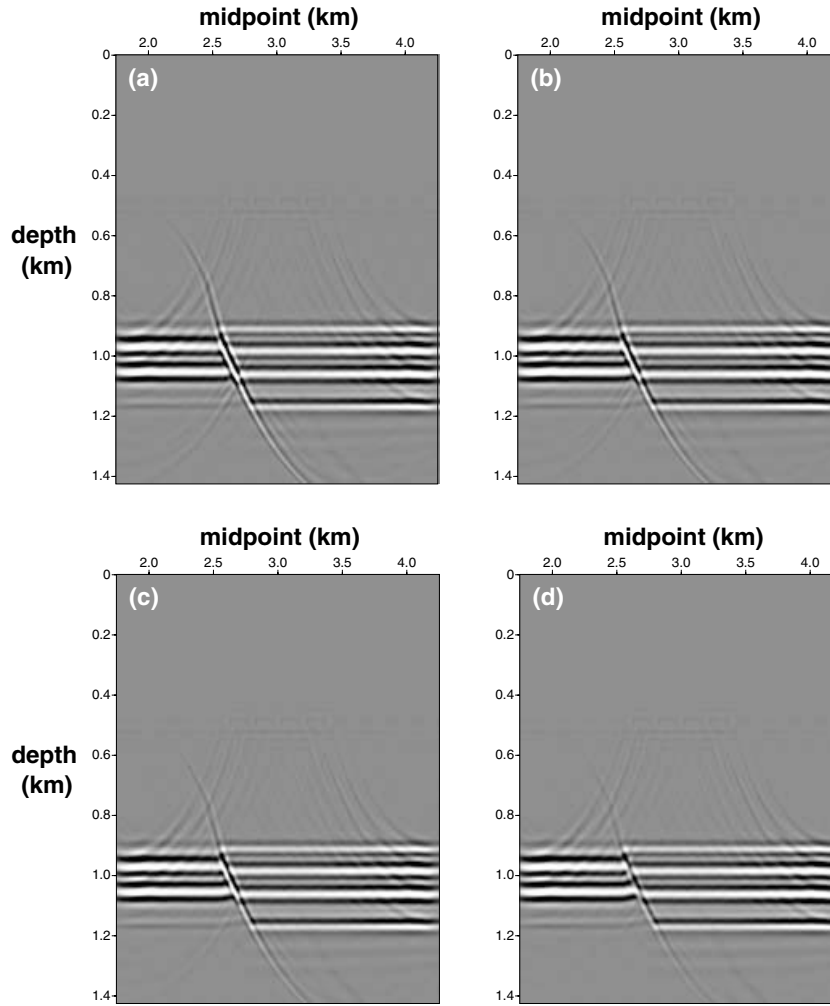$$\eta_N = -\frac{4h}{\rho\alpha\alpha_L} \ R_{PP}. \qquad (20)$$

Figure 11. Zero-offset migrated sections for Slip-Model A in panel (a), Slip-Model B in panel (b), Slip-Model C in panel (c) and Slip-Model D in panel (d). See Table 4 for a description of the different Slip-Models. All Slip-Models shown here are for a fault embedded in Model 2 (see Tables 1 and 2) having a pore-pressure contrast of 600 psi across the fault. The amplitude plots along the fault plane in Fig. 10 are derived from these zero-offset sections after dip-filtering.

In the weak scattering approximation, we can substitute a weak-scattering approximation for the normal-incidence welded-interface reflection coefficient R_{PP}. This can be obtained from eq. (A6) in the Appendix by ignoring the terms related to slip

$$R_{PP} = \frac{1}{2}\left(\frac{\Delta\rho}{\bar{\rho}} + \frac{\Delta\alpha}{\bar{\alpha}}\right), \tag{21}$$

where $\Delta\rho = \rho_L - \rho$, $\bar{\rho} = (\rho_L + \rho)/2$, $\Delta\alpha = \alpha_L - \alpha$ and $\bar{\alpha} = (\alpha_L + \alpha)/2$. Rewriting eq. (21) in terms of the properties of the layer and host medium gives

$$R_{PP} = \frac{\rho_L - \rho}{\rho_L + \rho} + \frac{\alpha_L - \alpha}{\alpha_L + \alpha}. \tag{22}$$

Substituting this expression into eq. (20) for R_{PP} yields

$$\eta_N = \frac{4h}{\rho\alpha\alpha_L}\left(\frac{\rho - \rho_L}{\rho + \rho_L} + \frac{\alpha - \alpha_L}{\alpha + \alpha_L}\right). \tag{23}$$

Since η_N is by definition greater than zero, the effective thin layer is allowed to have relatively lower density $\rho > \rho_L$ and lower velocity $\alpha > \alpha_L$ than the host medium. This is the case of a locally pressurized fault, since velocity and density decrease with increase in pore-pressure. We note that the weak-scattering approximation employed

here should be appropriate for *PP* reflection from an overpressurized fault since, according to the pore-pressure relationships described earlier, $\alpha_L \to 0$ does not occur for any value of the pore-pressure. This may not be the case for shear waves, though, since the shear wave velocity can go to nearly zero at zero effective stress (Zimmer *et al.* 2002).

Using the effective–stress relationships derived in previous sections for ρ_L and α_L in the case of unloading, $\rho_L^u(\sigma_d)$ and $\alpha_L^u(\sigma_d)$, and fixing the depth (or, equivalently the lithostatic stress σ_v) so that the effective stress varies only with pore-pressure ($\sigma_d = \sigma_v - p$), the compliance of a fracture can be put in terms of the thickness of the layer and the pore-pressure

$$\eta_N(h, P) = \frac{4h}{\rho\alpha\alpha_L^u(P)}\left[\frac{\rho - \rho_L^u(P)}{\rho + \rho_L^u(P)} + \frac{\alpha - \alpha_L^u(P)}{\alpha + \alpha_L^u(P)}\right]. \tag{24}$$

Note that we use the unloading relationships for ρ_L and α_L. This is because a slip interface is indicative of a locally weak fault. The relative weakness is due to the fault being overpressured, where by overpressured we mean its effective elastic properties are modified by pore-pressure as seen in the well log data of the previous sections. The overpressure in a fault could perhaps be from pressurized

fluid migrating up the fault plane, as recently observed by Haney *et al.* (2005b). Hence, the correct pressure curve to use is the unloading curve, since the migrating fluid is entering the pore space and unloading the fault zone sediments. This detail has also been discussed by Revil & Cathles (2002). The unloading curve requires an additional parameter, the maximum past effective stress σ_{max} that the fault rock has experienced before being unloaded to its current state. With this information, the slip models used in the previous modelling section can be related to an effective thin layer (or fault zone) described by four parameters: a fault zone of thickness h, fixed depth z, excess fluid pressure $P - P_h$ and maximum past effective stress σ_{max}.

Based on these considerations, the value of the pore-pressure corresponding to a particular linear-slip interface depends on three other parameters besides the pore-pressure. In Table 4, we fix two of these parameters—the depth of the fault zone (1850 m) and the thickness of the fault zone (10 m). We take the thickness of the fault based on the well logs that penetrated the B-fault zone. The table shows the values of the effective thin layer for each Slip-Model, A–D, while σ_{max} varies between 1600 and 2800 psi. The table also shows the effective stress corresponding to those values of velocity and density along the unloading path, and uses the assumed depth to convert the effective stress to pore-pressure. We do not show results for variation with thickness h since its effect is a simple linear scaling, as seen in eq. (23). The variation with depth z is also fairly unimportant since it changes only the value of the pore-pressure for a given effective stress. Note that, in Table 4, certain values of the compliance do not exist for some values of σ_{max} since the compliance does not fall in the range of possible compliances (i.e. it is not positive) based on the values of density and velocity. Hence, some small compliance values cannot be modelled for certain combinations of h, z and σ_{max}. In order to obtain smaller compliance values in these cases, the thickness of the fault would need to be made smaller because the compliance, from eq. (23), scales linearly with h.

In the A10ST well at South Eugene Island, the effective stress in the B-fault zone is measured to be as low as 166 psi (Losh *et al.* 1999), much lower than the effective stresses in the adjacent down or upthrown sediments. In other words, the fault itself is locally overpressured and weak compared to the host rock. Therefore, some of the low values for effective stress shown in Table 4, while unusual, are entirely possible for the growth faults at South Eugene Island. Anomalously low effective stresses of 575 and 807 psi were also measured in the A20ST well as it crossed the A-fault system (Losh *et al.* 1999). The locally high pore-pressures in the B-fault zone reported in Losh *et al.* (1999) have been implicated as the cause of anomalously high reflectivity observed at the B-fault plane (Haney *et al.* 2005b). Based on our numerical modelling, a plausible model for the B-fault zone in the location of the reported anomalously high reflectivity would be either Slip-Model A or B as shown in Table 4, for the case of $\sigma_{max} = 2000$ psi.

10 CONCLUSION

We have presented a complete numerical modelling experiment by utilizing an SEM implementation of the 2-D elastic wave equation and processing the resulting waveforms into their time-migrated images. We derived a simple dip filter and used it to isolate fault-plane reflections. We then exploited the relationships between the elastic parameters, density and velocity, to create physically meaningful models of sealing faults that maintain a ΔP of up to 600 psi. For these ΔP models, we assumed that the overpressure mechanism

is purely due to undercompaction. In the course of this modelling, we found that the minimum ΔP necessary to give rise to substantial fault-plane reflections is on the order of 150 psi at the South Eugene Island field. We have found evidence in field data arising from the lack of a reflection from the F-fault (see Fig. 1) supporting this estimate (Haney, 2005).

Taking advantage of the SEM modelling code's ability to accommodate linear-slip interfaces, we selected four different values of the normal and shear compliances for the fault interface. We found that the reflections from the slip interfaces dominate the reflections from pore-pressure contrasts across the fault for compliance values above $\sim 10^{-10}$ m Pa^{-1}. By noting that the different slip interfaces were in the weak scattering regime, we estimated the minimal values of the compliances necessary to produce a notable reflection at a fault without any ΔP across it. Looking for physical insight into the meaning of the slip interfaces, we derived, from a weak-scattering model, an equivalent thin, weak layer that gives virtually the same reflection as a linear-slip interface. We used this equivalent layer model to relate the slip interface to realistic values of pore-pressure in a fault zone at South Eugene Island. To do so required extensive use of the effective–stress relationships for the unloading paths derived from well logs at the South Eugene Island field.

Interpreting fault zone properties from fault-plane reflections is thus closely tied to knowledge of the subsurface distribution of fluids (Hatchell 2000) and stress histories. By paying attention to the details of the rock physics of pore-pressure and utilizing advanced numerical techniques for modelling wave propagation, the physical mechanisms giving rise to fault-plane reflections can be thoroughly investigated. Understanding the relative importance of these physical mechanisms makes possible the detection of fault properties through the prevalent techniques of seismic reflection imaging.

REFERENCES

Aki, K. & Richards, P., 1980. *Quantitative Seismology,* W.H. Freeman and Company, San Francisco.

Ampuero, J.P., 2002. Etude physique et numérique de la nucléation des séismes, *PhD thesis*, Université Paris 7, Paris, France.

Anderson, R.N., Flemings, P., Losh, S., Austin, J. & Woodhams, R., 1994. Gulf of Mexico growth fault drilled, seen as oil, gas migration pathway. *Oil Gas J.,* **92,** 97–103.

Andrews, D.J., 1999. Test of two methods for faulting in finite-difference calculations. *BSSA,* **89,** 931–937.

Athy, L.F., 1930. Density, porosity and compaction of sedimentary rocks. *AAPG Bull*. **14,** 1–22.

Bakulin, A., Grechka, V., Karaev, N., Anisimov, A. & Kozlov, E., 2004. Physical modeling and theoretical studies of seismic reflections from a fault zone. *SEG Int'l Exposition and 74th Annual Meeting,* Denver, Colorado, pp. 1674–1677, SEG.

Black, J.L., Schleicher, K.L. & Zhang, J., 1993. True-amplitude imaging and dip moveout. *Geophysics,* **58,** 47–66.

Boore, D.M., 1970. Finite-difference solutions to the equations of elastic wave propagation, with applications to Love waves over dipping interfaces, *PhD thesis*, MIT.

Bowers, G.L., 1995. Pore-pressure estimation from velocity data: accounting for overpressure mechanisms besides undercompaction. *SPE Drilling and Completion,* **10,** 89–95.

Carcione, J.M. & Tinivella, U., 2001. The seismic response to overpressure: a modeling study based on laboratory, well, and seismic data. *Geophys. Prospect.,* **49,** 523.

Chaisri, S. & Krebes, E.S., 2000. Exact and approximate formulas for $P - SV$ reflection and transmission coefficients for a nonwelded contact interface. *JGR,* **105,** 28045.

Coates, R.T. & Schoenberg, M., 1995. Finite-difference modeling of faults and fractures. *Geophysics,* **60,** 1514.

Crampin, S., Volti, T., Chastin, S., Gudmundsson, A. & Stefánsson, R., 2002. Indication of high pore-fluid pressures in a seismically-active fault zone. *Geophys. J. Int.,* **151,** F1–F5.

Dutta, N.C., 1997.Pressure prediction from seismic data: implications for seal distribution and hydrocarbon exploration and exploitation in the deepwater Gulf of Mexico, in *Hydrocarbon Seals: Importance for Exploration and Production,* pp. 187–199, eds Moeller-Pederson, P. & Koestler, A.G., Elsevier, Singapore.

Elliott, D.A., 1999. Hydrofracture Permeability response and maximum previous consolidation stress estimations for faulted and micro-faulted silty-shales taken from the Eugene Island Block 330 field Pathfinder Well in the Gulf of Mexico. *MSc thesis*, University of California, San Diego.

Engelder, T., 1993. *Stress Regimes in the Lithosphere,* Princeton University Press, Princeton.

Gurevich, B., 2004. A simple derivation of the effective stress coefficient for seismic velocities in porous rocks. *Geophysics,* **69,** 393–397.

Haney, M.M., 2005. An investigation of sealing and episodic pulsing of fluid at a minibasin-bounding growth fault from seismic reflection images. *Ph D thesis, Colorado School of Mines*.

Haney, M., Sheiman, J., Snieder, R., Naruk, S., Busch, J. & Wilkins, S., 2004. Fault-plane reflections as a diagnostic of pressure differences in reservoirs: a case study from South Eugene Island Block 330, in *Proceedings of the EAGE special session on Fault and Top Seals,* pp. O–07, eds Engelder, T., Konstanty, J. & Grauls, D., EAGE, Houten, The Netherlands.

Haney, M., Snieder, R. & Sheiman, J., 2005a. Further thoughts on the stacking response in seismic data processing. *First Break,* **23,** 35–38.

Haney, M.M., Snieder, R.J., Sheiman, S., Losh, 2005b. A moving fluid pulse in a fault zone. *Nature,* **437,** 46.

Hart, B.S., Flemings, P.B. & Deshpande, A., 1995. Porosity and pressure: role of compaction disequilibrium in the development of geopressures in a Gulf Coast Pleistocene basin. *Geology,* **23,** 45–48.

Hatchell, P.J., 2000. Fault whispers: transmission distortions on prestack seismic reflection data.*Geophysics,* **65,** 377.

Haugen, G.U. & Schoenberg, M., 2000. The echo of a fault or fracture. *Geophysics,* **65,** 176–189.

Hofmann, R., Xu, X., Batzle, M., Prasad, M., Furre, A.-K. & Pillitteri, A., 2005. Effective pressure or what is the effect of pressure? *The Leading Edge,* **24,** 1256–1260.

Hooper, E.C.D., 1991. Fluid migration along growth faults in compacting sediments. *J. Petol. Geol.,* **14,** 161–180.

Huffman, A.R. & Bowers, G.L., 2002. The future of pressure prediction using geophysical methods. *Pressure Regimes in Sedimentary Basins and Their Prediction,* pp. 217–233, eds Huffman,Alan, Bowers, Glenn, AAPG Memoir, no. 76. Tulsa: AAPG.

Jones, T.D. & Nur, A., 1984. The nature of seismic reflections from deep crustal fault zones. *JGR,* **89,** 3153–3171.

Karniadakis, G.E. & Sherwin, S.J., 1999. *Spectral/HP Element Methods for CFD,* Oxford University Press, Oxford.

Kelly, K.R., Ward, R.W., Treitel, S. & Alford, R.M., 1976. Synthetic seismograms: a finite-difference approach. *Geophysics,* **41,** 2.

Komatitsch, D. & Tromp, J., 1999. Introduction to the spectral-element method for three-dimensional seismic wave propagation. *Geophys. J. Int.,* **139,** 806.

Vlastos, S., Liu, E., Main, I.G. & Li.,X. Y., 2003. Numerical simulation of wave propagation in media with discrete distributions of fractures: effects of fracture sizes and spatial distributions. *Geophys. J. Int.,* **152,** 649–668.

Komatitsch, D. & Vilotte, J.P., 1998. The spectral element method: an efficient tool to simulate the seismic response of 2D and 3D geological structures. *BSSA,* **88,** 368–392.

Komatitsch, D., Barnes, C. & Tromp, J., 2000. Wave propagation near a fluid-solid interface: a spectral-element approach. *Geophysics,* **65,** 623–631.

Komatitsch, D., Ritsema, J. & Tromp, J., 2002. The Spectral-element method, beowulf computing, and global seismology. *Science,* **298,** 1737–1742.

Liner, C.L., 1999. *Elements of 3-D Seismology,* PennWell, Tulsa.

Losh, S., Eglinton, L., Schoell, M. & Wood, J., 1999. Vertical and lateral fluid flow related to a large growth fault. *AAPG Bull.,* **83,** 244–276.

Moore, J.C., Moore, G.F., Cochrane, G.R. & Tobin, H.J., 1995. Negative-polarity seismic reflections along faults of the Oregon accretionary prism: indicators of overpressuring. *JGR,* **100,** 12 895–12 906.

Nihei, K., Myer, L.R., Cook, N.G.W. & Yi, W., 1994. Effects of non-welded interfaces on guided *SH*-waves. *Geophys. Res. Lett.,* **21,** 745–748.

Oppenheim, A.V. & Schafer, R.W., 1975. *Digital Signal Processing,* Prentice-Hall, Englewood Cliffs, New Jersey.

Pennebaker, E.S., 1968. Seismic data indicate depth, magnitude of abnormal presures. *World Oil,* **166,** 73.

Pyrak-Nolte, L., Myer, L. & Cook, N., 1990. Transmission of seismic waves across single natural fractures. *JGR,* **95,** 8617–8638.

Revil, A. & Cathles, L.M., 2002. Fluid transport by solitary waves along growing faults: a field example from the South Eugene Island Basin, Gulf of Mexico. *Earth planet. Sci. Lett.,* **202,** 321–335.

Robinson, E.A., 1984. Statistical pulse compression. *Proceedings of the IEEE,* **72,** 1276–1289.

Schoenberg, M., 1980. Elastic wave behavior across linear slip interfaces. *J. Acoust. Soc. Am.,* **68,** 1516–1521.

Seriani, G. & Priolo, E., 1994. Spectral element method for acoustic wave simulation in hetrogeneous media. *Finite Elements Anal. Des.,* **16,** 337–348.

Stockwell, Jr., J.W., 1997. Free software in education; a case study of CWP7SU: seismic Unix. *The Leading Edge,* **16,** 1045–1049.

Stump, B., Flemings, P., Finkbeiner, T. & Zoback, M., 1998. Pressure differences between overpressured and bounding shales of the Eugene Island 330 field (offshore Louisiana, USA) with implications for fluid flow induced by sediment loading, in *Overpressures in Petroleum Exploration: Workshop Proceedings,* eds Mitchell, A. & Grauls, D., Elf Exploration Production Memoir 22.

Stump, B.B. & Flemings, P.B., 2002. Consolidation state, permeability, and stress ratio as determined from uniaxial strain experiments on mudstone samples from the Eugene Island 330 Area, offshore Louisiana, in *Pressure regimes in sedimentary basins and their prediction,* pp. 131–144 (eds) Huffman, A.R. & Bowers, G.L., AAPG Memoir, no. 76. Tulsa: AAPG.

Terzaghi, K., 1943. *Theoretical Soil Mechanics,* Wiley, New York.

Thompson, L.L. & Pinksy, P.M., 1994. Complex wavenumber fourier analysis of the p-version finite element method. *Computat. Mech.,* **13,** 255–275.

Townsend, C., Firth, I.R., Westerman, R., Kirkevollen, L., Harde, M. & Anderson, T., 1998. Small seismic-scale fault identification and mapping, in *Faulting, Fault Sealing and Fluid Flow in Hydrocarbon Resrvoirs,* eds Jones, G., Fisher, Q.J. & Knipe, R.J., Geological Society Special Publication No. 147.

Wang, H.F., 2000. *Theory of Linear Poroelasticity,* Princeton University Press, Princeton.

Widess, M.B., 1973. How thin is a thin bed? *Geophysics,* **38,** 1176–1180.

Worthington, M.H., 2006. The visibility of fluid-filled macro-fractures. in *12th International Workshop on Seismic Anisotropy,* Beijing, China, 12IWSA.

Worthington, M.H. & Hudson, J.A., 2000. Fault properties from seismic Q. *Geophys. J. Int.,* **143,** 937–944.

Worthington, M.H. & Lubbe, R., 2007. The scaling of fracture compliance. in *Fractured Reservoirs,* eds Lonergan, L., Jolly, R.J.H., Sanderson, D.J. & Rawnsley, K., Geological Society Special Publication No. 270.

Yilmaz, Ö., 1987. *Seismic Data Processing,* Society of Exploration Geophysicists, Tulsa.

Zhu, Y. & Snieder, R., 2002. Reflected and transmitted waves from fault zones, in *SEG Int'l Exposition and 72nd Annual Meeting, Salt lake City, Utah,* pp. 2273-2276, SEG.

Zienkiewicz, O.C. & Taylor, R.L., 2000. *The Finite Element Method,* Vol. 1, Butterworth-Heinemann, Oxford.

Zimmer, M., Prasad, M. & Mavko, G., 2002. Pressure and porosity influences on V_{P-V_S} ratio in unconsolidated sands. *The Leading Edge,* **21,** 178–183.

APPENDIX A: SPECTRAL ELEMENT MODELLING OF A LINEAR-SLIP INTERFACE

We chose the SEM to simulate fault reflectivity for its ability to allow a free-form mesh and in order to include the possibility of slip at interfaces in our numerical models. As evidence of SEM's ability to handle challenging boundary conditions, it has recently been applied to wave propagation near a fluid–solid interface (Komatitsch *et al.* 2000). Interfacial slip had been implemented previously in SEM2DPACK, the 2-D SEM code available online at the Orfeus Seismological Software Library: http://www.orfeus-eu.org/links/softwarelib.htm. SEM2DPACK was developed by one of the authors, J.-P. Ampuero, for the simulation of earthquake dynamics (Ampuero 2002). In this work, we adapted the interface condition to a linear-slip law.

For incident *P–SV* waves, the linear-slip law is a boundary condition expressed as (Schoenberg 1980)

$$\mathbf{t} \cdot \hat{\mathbf{n}} = \mathbf{Z}^{-1} \Delta \mathbf{u} \tag{A1}$$

$$\Delta \mathbf{u} = \begin{bmatrix} u_z^+ - u_z^- \\ u_x^+ - u_x^- \end{bmatrix}, \quad \mathbf{Z}^{-1} = \begin{bmatrix} \eta_T^{-1} & 0 \\ 0 & \eta_N^{-1} \end{bmatrix},$$

$$\mathbf{t} = \begin{bmatrix} \sigma_{xx} & \sigma_{xz} \\ \sigma_{xz} & \sigma_{zz} \end{bmatrix}, \quad \hat{\mathbf{n}} = \begin{bmatrix} 0 \\ 1 \end{bmatrix}, \tag{A2}$$

where the superscript $(-)$ refers to the side of the interface on which the wave is incident, $(+)$ the other side of the interface, u_x and u_z are the horizontal and vertical particle displacements, σ_{xx} and σ_{zz} are the normal stresses and σ_{xz} is the shear stress. The particular choice of the normal vector in eq. (A2) means that we consider here a horizontal slip interface. The SEM code has no such restriction; any orientation of a slip interface can be handled. The matrix $\mathbf{Z}^{-1}$ appearing in eqs (A1) and (A2) is the stiffness matrix of the slip interface (inverse of the compliance matrix). The fact that $\mathbf{Z}^{-1}$ is diagonal means we only consider rotationally symmetric slip interfaces (Haugen & Schoenberg 2000) in our SEM implementation. The parameters η_N and η_T are the normal and tangential compliances, respectively, and these quantify the degree of slip along the interface. For $\eta_N = 0$ and $\eta_T = 0$, the interface is welded, and for $\eta_N = \infty$ and $\eta_T = \infty$, it is a stress free surface.

The boundary condition described by eqs (A1) and (A2) can be obtained in the limit of a thin, weak layer in welded contact with its surrounding rock. As a result, linear-slip has been suggested as a good model for scattering from faults and fractures (Coates & Schoenberg 1995). With this in mind, it is important not to confuse the slip model in eqs (A1) and (A2) with slip that occurs along a fault during an earthquake. The linear-slip model entails some slipping at the interface that is the order of particle displacements during the passage of a seismic wave ($\sim 10^{-6}$ m). Active, earthquake-generating faults typically slip on a length scale three to four orders of magnitude larger ($\sim 10^{-3}$–10^{-2} m). Earthquake slip is also hysteretic, whereas interfaces undergoing linear-slip return to their equilibrium state after the seismic wave has moved on.

To implement the linear-slip model in SEM, the weak form of the equation of motion is needed (Komatitsch & Tromp 1999)

$$\int_\Omega \rho \mathbf{w} \cdot \partial_t^2 \mathbf{u} \, d^3\mathbf{x} = - \int_\Omega \nabla \mathbf{w} : \mathbf{t} \, d^3\mathbf{x} + \int_\Gamma [\mathbf{t} \cdot \hat{\mathbf{n}}] \cdot \mathbf{w} \, d^2\mathbf{x}, \tag{A3}$$

where $\mathbf{u}$ is the displacement, ρ is the density, $\mathbf{t}$ is the stress tensor, $\mathbf{t} \cdot \hat{\mathbf{n}}$ is the traction on the slip interface, and $\mathbf{w}$ is the test function. The semi-colons in eq. (A3) represent tensor contraction. The last term on the right-hand side of eq. (A3) is the contribution from the slip interface Γ, which is here taken to be planar. At the slip interface, we employ split nodes (Andrews 1999) in the spectral element mesh to accurately model a fracture.

After discretizing the displacement field and assembling the global mass and stiffness matrices, eq. (A3) can be written as the matrix equation (Komatitsch & Tromp 1999)

$$M\ddot{U} = -KU + BT, \tag{A4}$$

where M and K the mass and stiffness matrices, respectively, U is the displacement vector of the global system, and T is the traction vector of the global system. The last term is non-zero only on the part of the boundary where slip occurs; this restriction is imposed by the matrix B. The essence of this SEM implementation of a slip interface is that the two separate meshes on either side of the slip interface (denoted here as mesh 1 and mesh 2) are put into communication via the last term in eq. (A4) by using the slip law in eq. (A1)

$$M_1 \ddot{U}_1 = -K_1 U_1 + \eta_N^{-1} B_1 \Delta U_1^z + \eta_T^{-1} B_1 \Delta U_1^x$$
$$M_2 \ddot{U}_2 = -K_2 U_2 - \eta_N^{-1} B_2 \Delta U_2^z - \eta_T^{-1} B_2 \Delta U_2^x, \tag{A5}$$

where the asymmetry of the $\pm$ signs between the two last terms is in accordance with Newton's third law. The subscripts 1 and 2 indicate to which mesh the variables belong. The superscripts z and x label the normal and tangential component of the displacement discontinuity. In the formulation we have outlined here, the slip law, eq. (A1), enters into the equation of motion by a substitution of the slip for the traction at the fault. Note that, due to the compliance of the slip interface appearing in the denominator of eq. (A5), the numerical scheme experiences conditional instability for too small a compliance.

The SEM implementation of eq. (A5) utilizes an explicit Newmark scheme (Zienkiewicz & Taylor 2000) consisting of a predictor, a solver and a corrector step (Komatitsch & Vilotte 1998) as shown in Table (A1). Waveforms computed with this implementation are displayed in Fig. A1. Our model for this example is an elongated 2-D block, whose side boundaries, shown as dashed in Fig. A1, are periodic and whose upper and lower boundaries are absorbing. Consistent with the periodic boundary condition, we excite a unidirectional plane *P* wave near the top of the block. In front of the plane wave, we measure the wavefield with ten receivers. A slip

---

Since Chaisri & Krebes (2000) have previously solved for the frequency-dependent reflection coefficient from a slip interface, we can check our numerical result against the analytic solution. In the case of weak elastic contrasts across the slip interface, small (dimensionless) compliances, and small angles of incidence, the linearized *PP*-reflection coefficient at a planar slip interface is a good approximation to the true reflection coefficient. The *PP*-reflection coefficient in this case is given by:

$$R_{PP} \approx \left[\frac{1}{2} - 2\left(\frac{\beta}{\alpha}\right)^2 \sin^2\theta\right] \frac{\Delta\rho}{\rho} + \frac{1}{2} s^2\theta \frac{\Delta\alpha}{\alpha}$$

$$- 4\left(\frac{\beta}{\alpha}\right)^2 \sin^2\theta \frac{\Delta\beta}{\beta} + i\left[\frac{1}{2} - 2\left(\frac{\beta}{\alpha}\right)^2 \sin^2\theta\right] s\theta\omega\eta_N\rho\alpha$$

$$- 2i\left(\frac{\beta}{\alpha}\right)^3 \cos\theta\sin^2\theta\omega\eta_T\rho\beta, \tag{A6}$$

where $\Delta\alpha$, $\Delta\beta$ and $\Delta\rho$ are the changes in *P*-, *S*-wave velocity and density of the two half-spaces, α, β and ρ are the average *P*-, *S*-wave velocity and density of the two half-spaces, ω is the angular frequency of the incident wave, η_T and η_N are the tangential and normal

compliances of the interface, and θ is the reflection/incidence angle. As previously stated, the approximation in eq. (A6) holds for small relative changes in the medium parameters ($\Delta\alpha/\alpha$, $\Delta\beta/\beta$, $\Delta\rho/\rho \ll 1$), small dimensionless shear compliance ($\omega\eta_I\rho\beta \cos\theta \ll 1$), small dimensionless normal compliance ($\omega\eta_T\rho\alpha \sec\theta \ll 1$), and small angles of incidence. Note that, for the case of small dimensionless compliances, the reflected wave due to a pure slip interface between two identical half-spaces is proportional to the derivative of the incident wave.

We plot the wavefield interacting with the slip interface at each of the 10 receivers in Fig. A1. For the value of slip used in this example (2.2×10^{-9} m Pa^{-1}), the dimensionless normal compliance is relatively small and the reflection from the slip interface is well approximated by eq. (A6). We show a quantitative benchmarking between the numerically calculated reflection coefficient (shown by circles) and the exact theoretical reflection coefficient (depicted by the solid line) in the lower panel of Fig. A1. The agreement between the two curves supports the numerical implementation for slip interfaces used in this paper. The approximate expression for the reflection coefficient, eq. (A6), is shown in Fig. A1 as a dashed line and is seen to become a worse approximation with increasing frequency.